

1 **A network of CD163⁺ macrophages monitors enhanced permeability at the blood-dorsal
2 root ganglion barrier**

3

4 **Authors**

5 Harald Lund^{1*}, Matthew Hunt^{1*}, Zerina Kurtovic^{1,2*}, Katalin Sandor¹, Noah Fereydouni³,
6 Anais Julien⁴, Christian Göritz⁴, Jinming Han^{5,6}, Keying Zhu⁵, Robert A. Harris⁵, Jon Lampa³,
7 Lisbet Haglund⁷, Tony L. Yaksh⁸, Camilla I. Svensson^{1#}

8

9 ¹Department of Physiology and Pharmacology, Center for Molecular Medicine, Karolinska
10 Institutet, Stockholm, Sweden.

11 ²Kancera AB, Karolinska Institutet Science Park, Stockholm, Sweden

12 ³Department of Medicine, Rheumatology Unit, Center for Molecular Medicine, Karolinska
13 Institutet, Karolinska University Hospital, Stockholm, Sweden.

14 ⁴Department of Cell and Molecular Biology, Karolinska Institutet, Stockholm, Sweden.

15 ⁵Department of Clinical Neuroscience, Karolinska Institutet, Center for Molecular Medicine,
16 Karolinska University Hospital, Stockholm, Sweden.

17 ⁶Present address: Department of Neurology, Xuanwu Hospital, Capital Medical University,
18 Beijing, China.

19 ⁷Department of Surgery, Division of Orthopaedic Surgery, McGill University, Montreal, QC,
20 Canada.

21 ⁸Department of Anesthesiology, University of California, San Diego, La Jolla, CA. USA

22

23 *These authors contributed equally

24

25 # Corresponding author

26 Email: camilla.svensson@ki.se; Telephone: +46 8 524 87948; Fax: +46 8 310622

27 Address: Karolinska Universitetssjukhuset, CMM L8:03, 17176 Stockholm

28

29

30 **Abstract**

31 In dorsal root ganglia (DRG), macrophages reside in close proximity to sensory neurons, and
32 their functions have largely been explored in the context of pain, nerve injury and repair. In
33 this study, however, we discovered that the majority of macrophages in DRGs are in direct
34 contact with the vasculature where they constantly monitor the circulation, efficiently
35 phagocytosing proteins and macromolecules from the blood. Characterization of the DRG
36 endothelium revealed a specialized vascular network spanning the arteriovenous axis, which
37 gradually transformed from a barrier type endothelium in arteries to a highly permeable
38 endothelium in veins. Macrophage phagocytosis spatially aligned with peak endothelial
39 permeability and we identified caveolar transcytosis as a mechanism regulating endothelial
40 permeability. Profiling of the DRG immune landscape revealed two subsets of perivascular
41 macrophages with distinct transcriptome, turnover and function. CD163 expressing
42 macrophages self-maintained locally, specifically participated in vasculature monitoring,
43 displayed distinct responses during peripheral inflammation and were conserved in mouse and
44 Man. Our work provides a molecular explanation for the permeability of the blood-DRG
45 barrier and identifies an unappreciated role of macrophages as integral components of the
46 DRG-neurovascular unit.

47

48

49

50

51 **Introduction**

52 Tissue-resident macrophages are multi-functional and highly plastic immune cells that are
53 found in every organ of the body. A core function of macrophages shared across most organs
54 is to act as tissue sentinels and scavengers, by phagocytosing cellular debris and orchestrating
55 tissue repair. In addition, macrophages participate in more complex, tissue-specific processes,
56 as diverse as wiring of neural networks, production of blood vessels and bone as well as
57 turnover of dying cells or essential proteins in the liver, spleen and lung (Park et al., 2022;
58 Mass et al., 2023). It is now understood that such tissue-specialized functions are the result of
59 distinct molecular programs induced by microenvironmental cues (cell-contacts and secreted
60 molecules) in their tissues of residence (Gosselin et al., 2014; Lavin et al., 2014; Bonnardel et
61 al., 2019). Another factor contributing to macrophage variability in different organs relates to
62 their ontogeny. During development, organs are colonized by embryonic macrophages
63 derived from precursors in the yolk sac or fetal liver that can self-sustain throughout life
64 (Ginhoux et al., 2010; Schulz et al., 2012; Hoeffel et al., 2015; Perdiguero et al., 2015). By
65 contrast, there are subpopulations of macrophages identified in most tissues which require
66 constant replenishment from bone-marrow derived monocytes (Molawi et al., 2014; Shaw et
67 al., 2018; Dick et al., 2022).

68

69 Macrophages in the CNS are well-studied, where parenchymal microglia and border-
70 associated macrophages, residing in perivascular, meningeal and choroid plexus niches, are
71 recognized (Mildenberger et al., 2022). In the peripheral sensory nervous system, however,
72 aspects such as transcriptional heterogeneity, ontogeny, microenvironmental regulation and
73 homeostatic function are only starting to be explored (Kolter et al., 2020; Wang et al., 2020a;
74 Ydens et al., 2020). Macrophages associate with the entire length of sensory neurons, from
75 the distal peripheral nerve endings to the proximal processes entering the spinal column.
76 Macrophages are also prominent in dorsal root ganglia (DRG) (Zigmond and Echevarria,
77 2019), which are segmentally organized collections of sensory neuron cell bodies located
78 alongside the spinal cord. Transcriptional differences between macrophages residing in these
79 different locations are evident, indicating that they are a product of their endoneurial
80 microenvironment (Wang et al., 2020a). DRG macrophages increase in number during a
81 range of neuropathic conditions (Peng et al., 2016; Zhang et al., 2016; Vlist et al., 2022),
82 which may promote the development of pain (Yu et al., 2020; Raoof et al., 2021) or help
83 resolve it (Singh et al., 2022; Vlist et al., 2022). However, the homeostatic functions of
84 macrophages in the DRG have remained largely overlooked. Moreover, heterogeneity within
85 the macrophage pool, which is recognized in virtually every organ investigated, has not been
86 systematically examined in the DRG.

87

88 The axons of sensory neurons are protected from circulating toxic molecules and pathogens
89 by the blood-nerve barrier (BNB), which shares functional and morphological features with
90 the blood-brain barrier (BBB), including low levels of transcytosis, high expression of tight
91 junction proteins and lack of endothelial fenestrae (Ubogu, 2020). The neuronal cell bodies in
92 the DRG, however, are not only supplied by a denser vascular bed than the axons in the
93 peripheral nerve (Jimenez-Andrade et al., 2008), the endothelial cells within DRGs also have
94 significantly higher permeability (Olsson, 1968; Jacobs et al., 1976; Arvidson, 1979;
95 Kobayashi and Yoshizawa, 2002). Despite the long-standing appreciation for these properties,
96 an understanding of the mechanisms regulating endothelial permeability at the blood-DRG
97 barrier remain lacking. Furthermore, the role of macrophages in this context has remained
98 unexplored. Breakdown of endothelial barrier integrity occurs and contributes to disease
99 progression in a range of conditions affecting the BBB (Profaci et al., 2020) and the BNB
100 (Richner et al., 2019; Ubogu, 2020). The elevated permeability observed in DRG endothelium

101 makes the DRG susceptible to neurotoxic molecules, autoantibodies and infectious agents,
102 and is likely a major cause of sensory ganglionopathies, conditions leading to sensory loss or
103 painful manifestations (Amato and Ropper, 2020). Characterizing the cellular components of
104 the vascular niche and understanding how endothelial barrier integrity is maintained in the
105 DRG therefore remain important areas of research.
106

107 In this study we describe a dense network of perivascular macrophages residing in sensory
108 ganglia, tasked with monitoring the permeable blood-DRG barrier. Mechanistically, we found
109 that this process was driven by elevated caveolar transcytosis in endothelial cells coupled to a
110 self-sustained and highly phagocytic macrophage subset. Our work identifies a novel
111 immunovascular unit that has implications for understanding blood-nerve barrier homeostasis,
112 disease and therapy.
113

114

115 Results

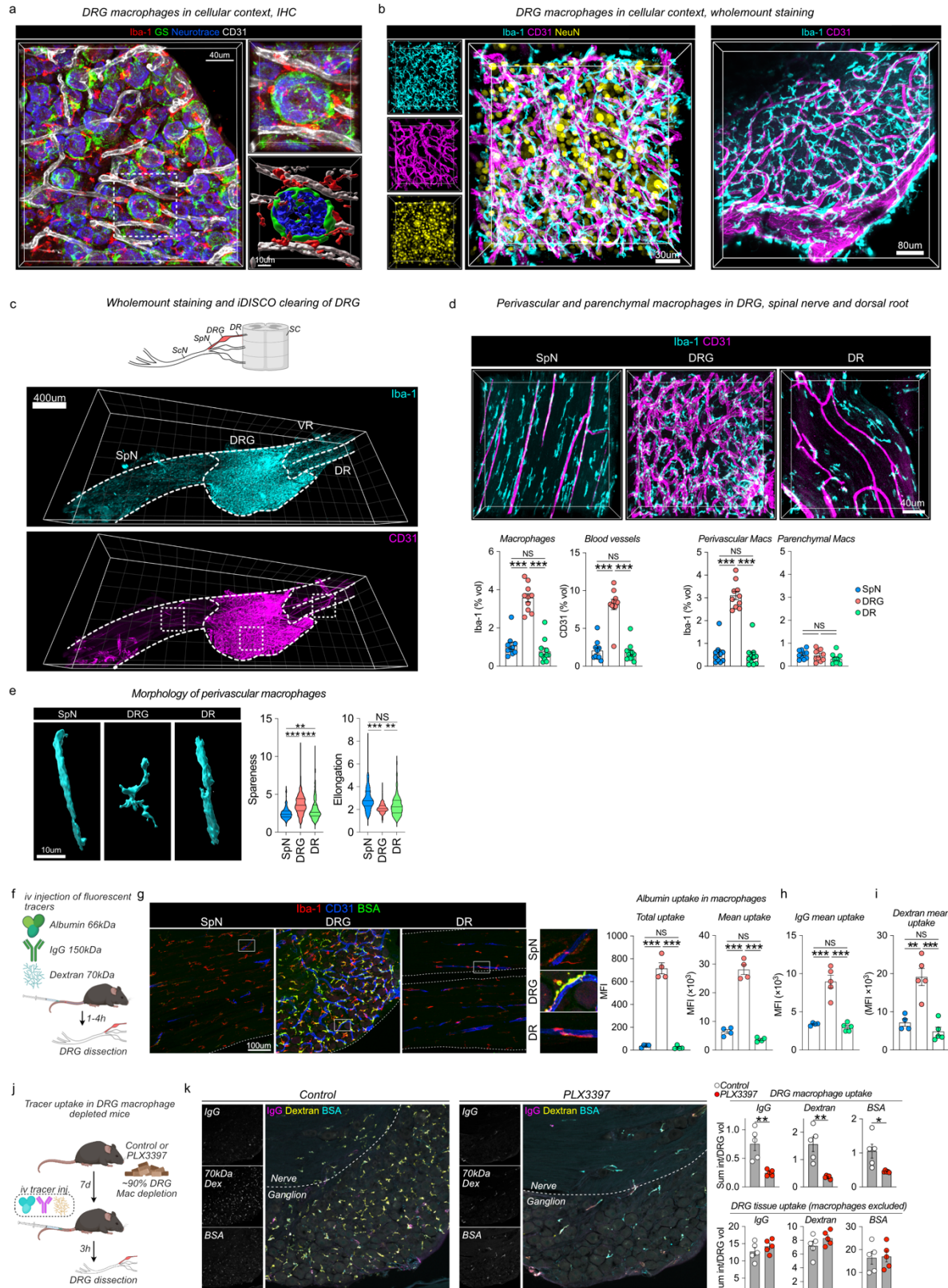
116

117 DRG macrophages monitor the vasculature

118 Macrophage functions are shaped by and tailored to their cellular microenvironment, known
119 as the ‘macrophage niche’ (Guilliams et al., 2020). To characterize the macrophage niche in
120 the DRG at a cellular level, we co-stained macrophages ($\text{Iba}1^+$) and major cell types in the
121 DRG, including neurons (Neurotrace $^+$), and satellite glial cells (SGC, GS $^+$) which wrap
122 around the neuronal soma (Hanani and Spray, 2020). Given the high degree of vascularization
123 in the DRG (Jimenez-Andrade et al., 2008), we also stained endothelial cells. This analysis
124 revealed that macrophages were positioned in the space between SGCs and endothelial cells
125 (Fig. 1a), often making close contact with endothelial cells (Fig. 1b). This prompted us to
126 further explore the interaction between macrophages and endothelial cells in the DRG.
127

128

129 We next stained Iba-1^+ macrophages and CD31^+ endothelial cells in DRG wholemounts,
130 followed by iDISCO tissue clearing and 3D-confocal imaging (Fig. 1c). DRGs were dissected
131 with the spinal nerve (SpN) and dorsal root (DR) attached, which allowed comparisons of
132 macrophages across these three tissue regions. Quantification of macrophage volume showed
133 a significant increase in the DRG compared to adjacently located SpN and DR (Fig. 1d). This
134 finding was confirmed using flow cytometry of enzymatically digested tissues, showing that
135 the DRG contained a higher number of $\text{CX3CR1}^+\text{CD64}^+$ macrophages than did the sciatic
136 nerve (ScN) per weight of tissue (Supplementary Fig. 1a). Comparison of the level of
137 vascularization similarly demonstrated a 4-fold increase in the DRG compared to the SpN and
138 DR (Fig. 1d), which supports previous findings (Jimenez-Andrade et al., 2008). We then
139 investigated the spatial relationship between endothelial cells and macrophages, observing
140 that macrophages that were in direct contact with the abluminal side of endothelial cells
141 (perivascular) were approximately 6-fold more prevalent in the DRG than in the DR or SpN
142 (Fig. 1d). Macrophages that did not make contact with the vasculature (parenchymal) were
143 similar in volume across the three tissue regions (Fig. 1d). The morphology of perivascular
144 DRG macrophages was also distinct, coiling around vessels and displaying a more tortuous
145 shape than did their SpN and DR counterparts. SpN and DR perivascular macrophages had a
146 more elongated shape, extending along blood vessels parallel to the axons (Fig. 1e). Our data
147 thus far demonstrate a local increase in perivascular macrophages specifically in the DRG.



148
149

150 Figure 1: DRG macrophages interact closely with the vasculature

151 (a) Representative immunostaining of neurons, SGCs, endothelial cells and macrophages in naive DRGs. (b) 3D confocal
152 images of DRG whole mounts to visualize neuron, macrophage and endothelial cells. (c) 3D Confocal images of iDISCO-
153 cleared whole mounts of DRGs with attached spinal nerve (SpN) and dorsal/ventral roots (DR/VR) stained with Iba-1 and
154 CD31. (d) Confocal Z-stacks of boxed areas in (c). Quantifications of macrophage and vascular density performed in
155 indicated regions. n=10, 10, 11 mice/group. Tukey's multiple comparisons test. (e) Morphology of perivascular macrophages
156 as measured by their sparseness (high value indicates spider-like shape) and elongation (high value indicates cigar-shape).

157 Tukey's multiple comparisons test. Experiment schematic of i.v injection of fluorescent tracers. (f) BSA-A647 uptake in Iba-
158 1⁺ macrophages 1h after i.v injection. N=4mice/group. The experiment was performed twice. Tukey's multiple comparisons
159 test. (g) Uptake of goat IgG-A488 (4mg/kg) in Iba-1⁺ macrophages 4h after i.v injection. N=4mice/group. The experiment
160 was performed twice. Tukey's multiple comparisons test. (h) Uptake of 70kDa dextran-TMR in Iba-1⁺ macrophages 2h45min
161 after i.v injection. The experiment was performed twice. 1-way ANOVA and Tukey post-hoc test. (i) Experiment schematic
162 of i.v tracer uptake in macrophage depleted mice using the CSF1R antagonist PLX3397 (290ppm in chow). Tukey's multiple
163 comparisons test. (j) Uptake of BSA-A647 (4 mg/kg) , 70kDa dextran-TMR (10mg/kg) and goat anti rabbit IgG-A488
164 (3mg/kg) in Iba-1⁺ macrophages or in DRG parenchyma (excluding macrophages) 2h45min after i.v injection. The
165 experiment was performed once. Student's unpaired t-test.
166
167

168 Given the well-described capacity of low and high molecular weight compounds to permeate
169 the blood-DRG barrier (Olsson, 1968; Jacobs et al., 1976; Arvidson, 1979; Kobayashi and
170 Yoshizawa, 2002), we next addressed whether macrophages had the capacity to phagocytose
171 circulating molecules. To that end we intravenously injected mice with either fluorescently
172 labeled albumin (BSA, 66kDa) or IgG (150 kDa), the two most abundant proteins in plasma.
173 Sacrificing animals within 1 hour (BSA) or 4 hours (IgG) revealed that both proteins readily
174 accumulated inside DRG macrophages and quantification across sensory nerve regions
175 demonstrated a 4-to-7 fold (BSA) or 2-fold (IgG) higher uptake in DRG macrophages
176 compared to in SpN or DR macrophages (Fig. 1f-h). To substantiate these findings we next
177 injected 70kDa dextran, a branched glucan used clinically as a plasma substitute that displays
178 minimal extravasation across the healthy BBB(Armulik et al., 2010). Similarly to our IgG and
179 BSA injections, dextran uptake was elevated in DRG macrophages compared to in SpN and
180 DR macrophages (Fig. 1i). Next we addressed whether DRG macrophages were actively
181 monitoring the circulation or only passively phagocytosing material leaking through the
182 blood-DRG barrier. Administration of the CSF1R-antagonist PLX3397 in chow resulted in
183 90% depletion of DRG macrophages within 7 days (Supplementary Fig. 1b, Fig. 1j) and as
184 expected, resulted in abrogation of vascular monitoring of IgG, dextran and BSA (Fig. 1k).
185 However, we did not observed increased tracer leakage into the DRG parenchyma (Fig. 1k),
186 indicating that macrophages were actively involved in the monitoring process. These results
187 demonstrate that the majority of DRG macrophages interact with the vasculature and monitor
188 the circulation for both endogenous and exogenous molecules.
189

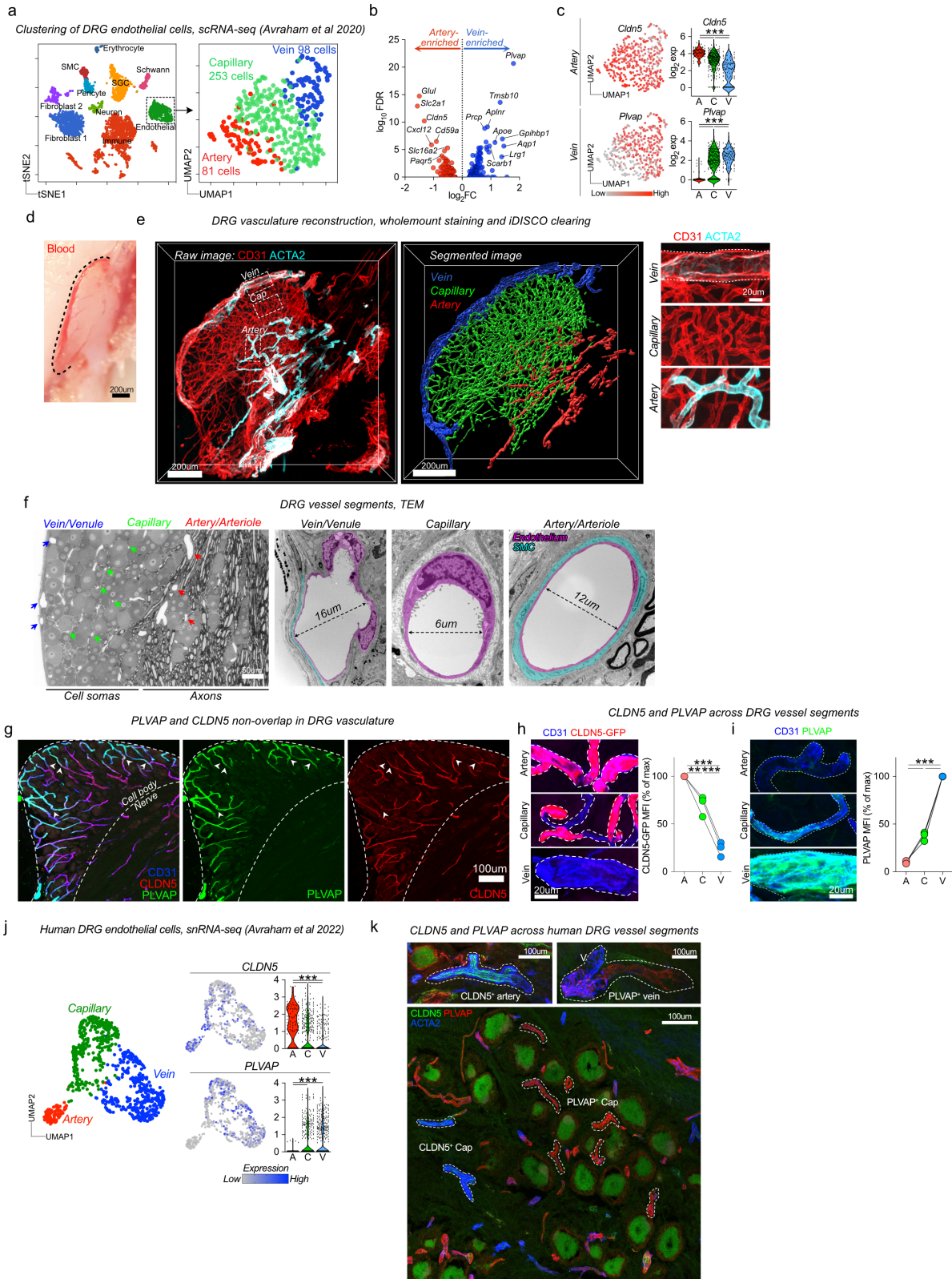
190 **The DRG vasculature displays both barrier and permeable properties and has a 191 conserved arteriovenous distribution**

192 While differences in vascular permeability between the blood-nerve and blood-ganglion
193 barrier are recognized (Reinhold and Rittner, 2020), an in-depth molecular understanding of
194 this phenomenon is lacking. We hypothesized that increased vascular permeability could at
195 least partly explain the level of circulating protein uptake in DRG macrophages, and we next
196 sought to better characterize DRG endothelial cells. Guided by a previous report (Munji et al.,
197 2019), we first analyzed whether DRG endothelial cells expressed markers specific to the
198 BBB or peripheral endothelium. This revealed that DRG endothelial cells expressed high
199 levels of the glucose transporter *Slc2a1* as well as the amino acid transporter *Slc7a5*, both
200 which are specific to the BBB (Munji et al., 2019; Kalucka et al., 2020). DRG endothelial
201 cells also expressed *Gpihbp1*, involved in lipid metabolism, and the prostaglandin transporter
202 *Slco2a1*, these genes normally being expressed in the kidney, liver and lung endothelium but
203 are absent from the BBB (Supplementary Fig. 2a). These results indicated that DRG blood
204 vessels expressed both peripheral and CNS-specific markers, and further suggested
205 transcriptomic heterogeneity across the DRG endothelial population.
206

207 Progressive transcriptomic changes along the arteriovenous axis, a process defined as
208 'zonation', has been recognized in several endothelial beds using scRNA-seq (Vanlandewijck

209 et al., 2018; Kalucka et al., 2020). To address transcriptomic zonation in the DRG
210 vasculature, we re-clustered a publicly available mouse scRNA-seq dataset (Avraham et al.,
211 2020) which included 432 DRG endothelial cells. Three clusters of endothelial cells were
212 identified (Fig. 2b), which we annotated as *artery*, *capillary* and *vein*, respectively, based on
213 expression of well-established (Vanlandewijck et al., 2018; Kalucka et al., 2020; Trimm and
214 Red-Horse, 2022) artery- (*Hey1*, *Bmx*, *Vegfc*, *Sema3g*) and vein-specific markers (*Nr2f2*, *Bgn*,
215 *Vcam1*, *Vwf*) in the two clusters that occupied the extremes of the UMAP (Supplementary
216 Fig. 2b). Differential gene expression further revealed that the artery cluster was characterized
217 by high expression of *Cldn5*, *Slc2a1* and *Mfsd2a*, which are all highly enriched in brain
218 endothelial cells (Supplementary Fig. 2c-d). *Cldn5* encodes a tight junction protein which
219 maintains BBB integrity (Greene et al., 2019) and *Mfsd2a* is a transporter of essential fatty
220 acids required for proper brain development and function (Nguyen et al., 2014). The vein
221 cluster displayed high expression of *Plvap*, *Aqp1*, *Gpihbp1* and *Lrg1*, all being enriched in
222 peripheral endothelial beds (Supplementary Fig. 2c-d). *Plvap* encodes a protein restricted to
223 endothelial fenestrae, transendothelial channels and caveolar vesicles; structures involved in
224 microvascular permeability (Guo et al., 2016). All these markers, including *Plvap* and *Cldn5*,
225 displayed a zonated expression profile, peaking in either arteries or veins and gradually
226 decreasing or increasing along the arteriovenous axis (Fig. 2c).

227 We next wanted to validate these markers at the protein level. In order to anatomically
228 identify the three vessel segments we stained CD31 and smooth muscle actin (SMA/ACTA2)
229 in DRG wholemounts and used 3D-confocal imaging to reconstruct the DRG vasculature.
230 This analysis revealed a conserved anatomical distribution, where arteries entered the neuron-
231 rich region from the nerve fiber, giving rise to a capillary bed that was subsequently collected
232 into veins on the DRG surface (Fig. 2d-e). Transmission electron microscopy (TEM) further
233 validated the anatomical location of these vessel segments (Fig. 2f). We explored the
234 expression of the two top artery- and vein-markers, *Cldn5* and *Plvap*, at the protein level. Co-
235 staining in DRG sections revealed that both markers were restricted to endothelial cells, but
236 with minimal overlap, PLVAP being expressed in superficially located vessels and CLDN5 in
237 those closer to the nerve fiber (Fig. 2g). Using *Cldn5*^{GFP/+} mice we could confirm high
238 expression of CLDN5 in ACTA2⁺ arteries, intermediate expression in capillaries, and
239 complete absence in large veins on the DRG surface (Fig. 2h, Supplementary Fig. 2e,
240 Supplementary Fig. 2g). This pattern was completely reversed for PLVAP, which displayed
241 the highest expression in large veins, intermediate expression in capillaries whereas ACTA2⁺
242 arteries were completely devoid of PLVAP expression (Fig. 2i, Supplementary Fig. 2f). The
243 presence of CLDN5-PLVAP⁺ capillaries entering the endoneurium appeared unique to the
244 DRG, as it was not observed in the SpN or ScN, where CLDN5-PLVAP⁺ vessels were
245 restricted to the epineurium (Supplementary Fig. 2h). Our results reveal that the DRG
246 arteriovenous tree has a predictable anatomical localization and is distinguished by a gradual
247 phenotypic shift characterized by loss of barrier properties and gain of permeability
248 properties.



250
251

252 Figure 2: DRG vasculature has dual identity

253 (a) Analysis of 432 endothelial cells from Avraham et al displaying clusters with artery, capillary and vein identity. (b)
254 Differential gene expression between artery and vein clusters using Venice algorithm. (c) *Cldn5* (artery) and *Plvap* (vein)
255 expression across clusters. (d) Photomicrograph of undissected L5 DRG from unperfused mouse illustrating blood-filled
256 vasculature. (e) Whole mount imaging and iDISCO tissue-clearing of CD31 and ACTA2 on lumbar DRG. 3D-reconstruction
257 and vessel segment identification using Imaris. (f) Identification of vessel segments in ultrathin DRG sections by TEM, based
258 on their anatomical localization. (g) CLDN5 and PLVAP expression in CD31⁺ DRG endothelial cells, displaying minimal

259 overlap. Arrows indicate PLVAP/CLDN5 breakpoints. (h) Mean CLDN5 expression in DRG vessel segments, normalized to
260 % of max. n=3 mice. Tukey's multiple comparisons test. (i) Mean PLVAP expression in DRG vessel segments, normalized
261 to % of max. n=3 mice. Tukey's multiple comparisons test. (j) Clustering of 777 endothelial cells from human DRGs from 5
262 donors (Avraham et al 2022) and the expression of *CLDN5* and *PLVAP* across artery, capillary and vein clusters. (k)
263 Immunostaining of CLDN5 and PLVAP in human DRG sections. A= artery. V=vein. Cap = Capillary

264
265

266 **Arteriovenous zonation is conserved in human DRG vasculature**

267 Human DRGs have higher *in vivo* blood perfusion rates than the SpN as measured by fMRI
268 (Godel et al., 2016), suggesting that DRG endothelial permeability is a feature shared between
269 mouse and Man. However, the vasculature has not previously been studied in detail in human
270 DRGs. We thus sought to address whether human DRGs displayed a similar profile as in
271 mouse. We first analyzed a recently published snRNA-seq dataset of human DRGs (Avraham
272 et al., 2022), which included one cluster of 777 *PECAMI*⁺ (encoding CD31) endothelial cells.
273 Subclustering of endothelial cells revealed three distinct clusters that could be assigned vein,
274 capillary and artery annotations, based on expression of artery (*GJA5*, *SEMA3G*, *VEGFC*) and
275 vein (*NR2F2*, *KCNIP4*, *IL1R1*) enriched markers identified in other organs (Supplementary
276 Fig. 2i) (Chen et al., 2022; Trimm and Red-Horse, 2022; Yang et al., 2022). Exploring the top
277 barrier and permeability markers identified in mouse DRG endothelial cells, *CLDN5* and
278 *PLVAP*, revealed that both genes were zonated and similarly enriched in arteries and veins,
279 respectively (Fig. 2j). Using DRG tissues collected from human organ donors of varying sex
280 and age (Supplementary Table 1), we validated CLDN5 expression in ACTA2⁺ arteries and
281 arterioles and its absence from veins and most capillaries supplying the neuronal soma-rich
282 region (Fig. 2k). Consistent with the snRNA-seq data, PLVAP was absent from arteries, but
283 stained most capillaries supplying the neuronal soma-rich areas, as well as large veins in the
284 capsule (Fig. 2k). This indicates that the human DRG vasculature is also characterized by a
285 dual identity with barrier-type arteries and highly permeable veins.

286

287 **Macrophage monitoring of DRG vasculature is arteriovenously zonated and requires 288 caveolar transcytosis**

289 The zonated proteogenomic profile of the DRG vasculature next led us to address whether
290 endothelial permeability was variable along the arteriovenous axis. Using DRGQuant, a
291 machine-learning based algorithm that we recently developed to analyze DRG macrophages
292 in tissue sections (Hunt et al., 2022) we performed spatial mapping of macrophages along the
293 arteriovenous tree (Fig. 3a). We intravenously injected mice with a series of macromolecules
294 of different size including dextrans, albumin and IgG, ranging from 3 kDa to 2000 kDa, and
295 analyzed macrophage-mediated uptake and organized the data based on which vessel segment
296 the macrophages contacted. This demonstrated a gradual increase in macrophage uptake from
297 arteries to veins, consistently peaking in either venous capillaries (v-cap) or veins (Fig. 3a).
298 While the mean uptake in endothelial cells was lower than in macrophages, the uptake across
299 vessel segments mirrored that in macrophages (Supplementary Fig. 3a).

300

301 The DRG vasculature thus displayed arteriovenously zonated permeability which correlated
302 with the presence CLDN5-PLVAP⁺ endothelial cells. As PLVAP is restricted to endothelial
303 fenestrae, transendothelial channels and caveolae (Guo et al., 2016), we next sought to
304 quantify the presence of these substructures across DRG vessel segments using TEM. The
305 presence of fenestral openings in the DRG vasculature have been reported (Anzil et al.,
306 1976; Jacobs et al., 1976; Arvidson, 1979; Kobayashi and Yoshizawa, 2002), and we did
307 identify fenestrae which were virtually restricted to v-caps (Supplementary Fig. 3b), although
308 their numbers were limited (only 0.06% of endothelial lining). The overall scarcity of
309 fenestrae was further confirmed by scanning electron microscopy (SEM) visualization of the

310 inner lumen of DRG vessels (Supplementary Fig. 3c). We did not observe any
311 transendothelial channels in the DRG vasculature (data not shown). Using higher
312 magnification TEM images, we instead observed that small endothelial vesicles (~100nm),
313 likely caveolar vesicles, were ubiquitous in the DRG vasculature. Machine-learning based
314 image quantification revealed a significantly higher presence of such vesicles in v-caps and
315 veins compared to in arteries and arterial capillaries (a-caps) (Fig. 3b). We confirmed that
316 these vesicles were caveolar vesicles, as they were absent in the DRG endothelium from
317 *Cav1^{-/-}* mice (Supplementary Fig. 3d) which cannot form caveolae (Parton et al., 2020).
318 However, fenestrae were still present in DRG v-caps from *Cav1^{-/-}* mice (Supplementary Fig.
319 3d). To further understand the regulation of caveolae across DRG vessel segments we
320 quantified expression of CAV1, the main scaffolding protein required for caveolae assembly.
321 We also explored expression of MFSD2A, an inhibitor of caveolar transcytosis (Andreone et
322 al., 2017) which is restricted to barrier endothelium in the CNS, testis (Supplementary Fig.
323 3e) and retina (Wang et al., 2020b). We recorded high levels of Mfsd2a mRNA and protein in
324 DRG endothelial cells (Supplementary Fig. 3f-g), and that mRNA expression gradually
325 decreased from arteries to veins (Fig. 3c). Protein levels of MFSD2A were similarly zonated,
326 reaching a peak in a-caps and then gradually decreasing to negligible levels in veins (Fig. 3d,
327 Supplementary Fig. 3g, Supplementary Fig. 3i). *Cav1* was not zonated at the mRNA level
328 (Fig. 3c), but its protein level displayed an opposite pattern to that of MFSD2A, increasing
329 gradually from arteries to veins (Fig. 3d, Supplementary Fig. 3h, Supplementary Fig. 3j). This
330 suggested that CAV1 expression may be regulated by MFSD2A in the DRG vasculature,
331 which is observed at the BBB and blood-retinal barrier (Andreone et al., 2017; Wang et
332 al., 2020b).

333
334 To investigate if caveolar transcytosis was required for macrophage monitoring of DRG
335 endothelium, we used *Cav1^{-/-}* mice and injected BSA and IgG into the tail vein. DRG
336 macrophage uptake of intravenously injected IgG and BSA were both significantly reduced in
337 *Cav1^{-/-}* mice compared to in WT controls (Fig. 3e). When perivascular macrophages were
338 spatially mapped along the arteriovenous axis and analyzed based on which vessel segment
339 they contacted, the largest difference between WT and *Cav1^{-/-}* mice was noted in v-caps (Fig.
340 3e), which is consistent with the high level of caveolar vesicles observed in this location. This
341 indicated that perivascular macrophages were ingesting material passing across endothelial
342 cells via caveolar vesicles. In support of this hypothesis, using confocal and STED
343 microscopy, we observed that DRG macrophages made direct contact with the cell membrane
344 of CAV1⁺ v-caps (Fig. 3f-g). TEM further confirmed this notion, showing that macrophages
345 and endothelial cells made direct cell-to-cell contact in this location, without being separated
346 by a layer of extracellular matrix or basement membrane (Fig. 3h). Taken together, our data
347 demonstrate a structural zonation across the DRG vasculature that spatially aligns with its
348 permeability. Furthermore, caveolar transcytosis is at least partly required for monitoring of
349 the vasculature by DRG macrophages.
350

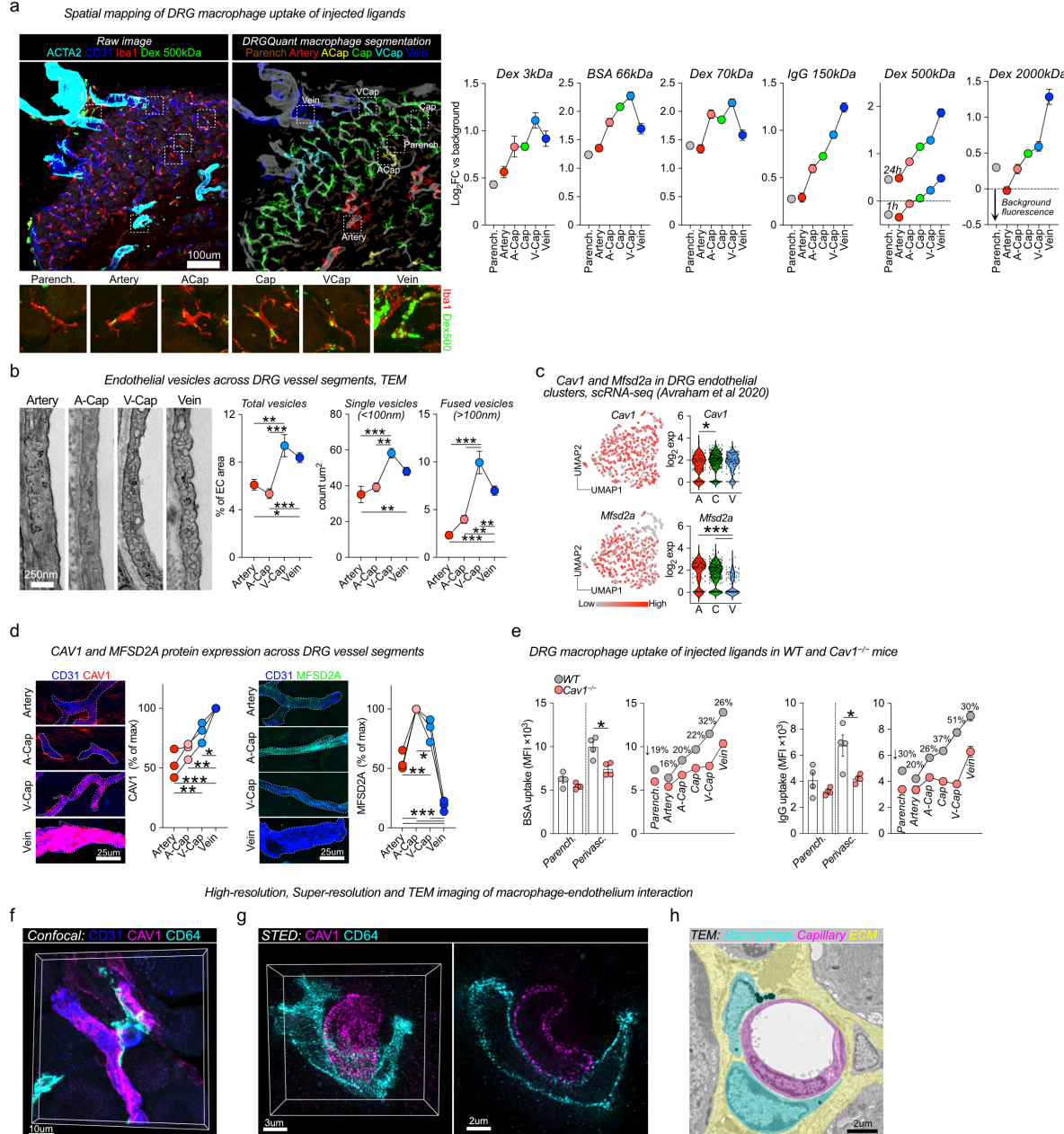


Figure 3: Macrophage monitoring is arteriovenously zoned and requires caveolar vesicles

(a) Machine learning-based spatial mapping of Iba-1⁺ macrophages to DRG vessel segments and analysis of uptake of indicated i.v.-injected tracers, using the DRGQuant algorithm. The following tracers, doses and circulation times were used: 3kDa dextran-TMR (25mg/kg, 1h, n=4 mice), BSA-A647 (5mg/kg, 1h, n=4 mice), 70kDa dextran TMR (25mg/kg, 1h, n=9 mice), goat anti rabbit IgG-A488 (4mg/kg, 4h, n=4 mice), 500kDa dextran-FITC (25mg/kg, 1h or 24h, n=4 mice), 2000kDa dextran-FITC (25mg/kg, 24h, n=4 mice). Values are mean of individual macrophages, normalized to tissue background. (b) Machine learning-based quantifications of endothelial vesicles (<100nm diameter) in high-resolution images of indicated DRG vessel segments. Data are mean of 50 (A), 51 (A-Cap), 42 (V-Cap) and 120 (V) images from n= 2 mice. Tukey's multiple comparisons test. (c) Expression of Cav1 and Mfsd2a mRNA in DRG vessel segments. Tukey's multiple comparisons test. (d) Immunostaining of CAV1 and MFSD2A in DRG sections, mean intensity analyzed in indicated vessel segments. n=3 mice Tukey's multiple comparisons test. (e) i.v injection of BSA-A488 (1mg/ml) and Goat IgG-A647 (1mg/ml) in WT and Cav1^{-/-} mice (n=4/group), sacrificed after 2h. Bar graphs are quantification of uptake in parenchymal and perivascular Iba-1⁺ macrophages. Line-connected graphs are quantifications of perivascular macrophages across endothelial vessel segments. Percentages indicate the reduction in macrophage-uptake between WT to Cav1^{-/-} mice at each vessel segment. Multiple unpaired t-test with Holm Sidak correction. (f) Confocal image of CD64⁺ macrophage with CAV1⁺ DRG blood vessel. (g) STED-captured Z-stack (left) and one Z-layer (right). (h) TEM image of macrophage-endothelial contact.

351
352

353
354
355
356
357
358
359
360
361
362
363
364
365
366
367
368
369
370
371

372

373 Two molecularly distinct subsets of macrophages inhabit the DRG

374 Our data thus far showed that macrophages in the DRG are predominantly perivascular,
375 highly phagocytic and ingest virtually all material crossing through ganglionic blood vessels.
376 These results indicate specialization of the macrophage population at the blood-DRG
377 interface, which prompted us to explore the DRG macrophage pool in greater detail. We used
378 scRNA-seq using the 10x platform to profile the DRG immune landscape at steady state (n=3
379 mice, 2668 cells). Using dimensionality reduction (UMAP) and unbiased clustering (Louvain)
380 we determined that the DRG was characterized by a heterogenous population of immune cells
381 which included neutrophils (*S100a8*, *S100a9*), monocytes (*S100a4*, *Plac8*), B-cells (*Cd79a*,
382 *Igkc*), T-cells (*Tbrc2*, *Cd3g*), dendritic cells (DCs) (*Xcr1*), but was numerically dominated by
383 macrophages (*C1qa*, *Csf1r*, *Cx3cr1*; 59% of all cells) (Fig. 4a), which separated into two
384 major clusters characterized by *Fcrls*, *Cd163*, *Mrc1* (47.2% of macrophages) or *Ccr2* and
385 *Cd52* expression (40.2% of macrophages), respectively. Three additional smaller macrophage
386 clusters were present, one displaying interferon-regulated gene expression (*Isg15*, *Ifi44*, *Irf7*;
387 6.4% of macrophages), one expressing stress-induced genes (*Prdx1*, *Ppia*; 5.4% of
388 macrophages) and one cluster expressing a core signature (*Timd4*, *Lyve1*, *Folr2*, TLF) of
389 embryonically-derived self-renewing macrophages (Dick et al., 2022) (0.7% of
390 macrophages).

391

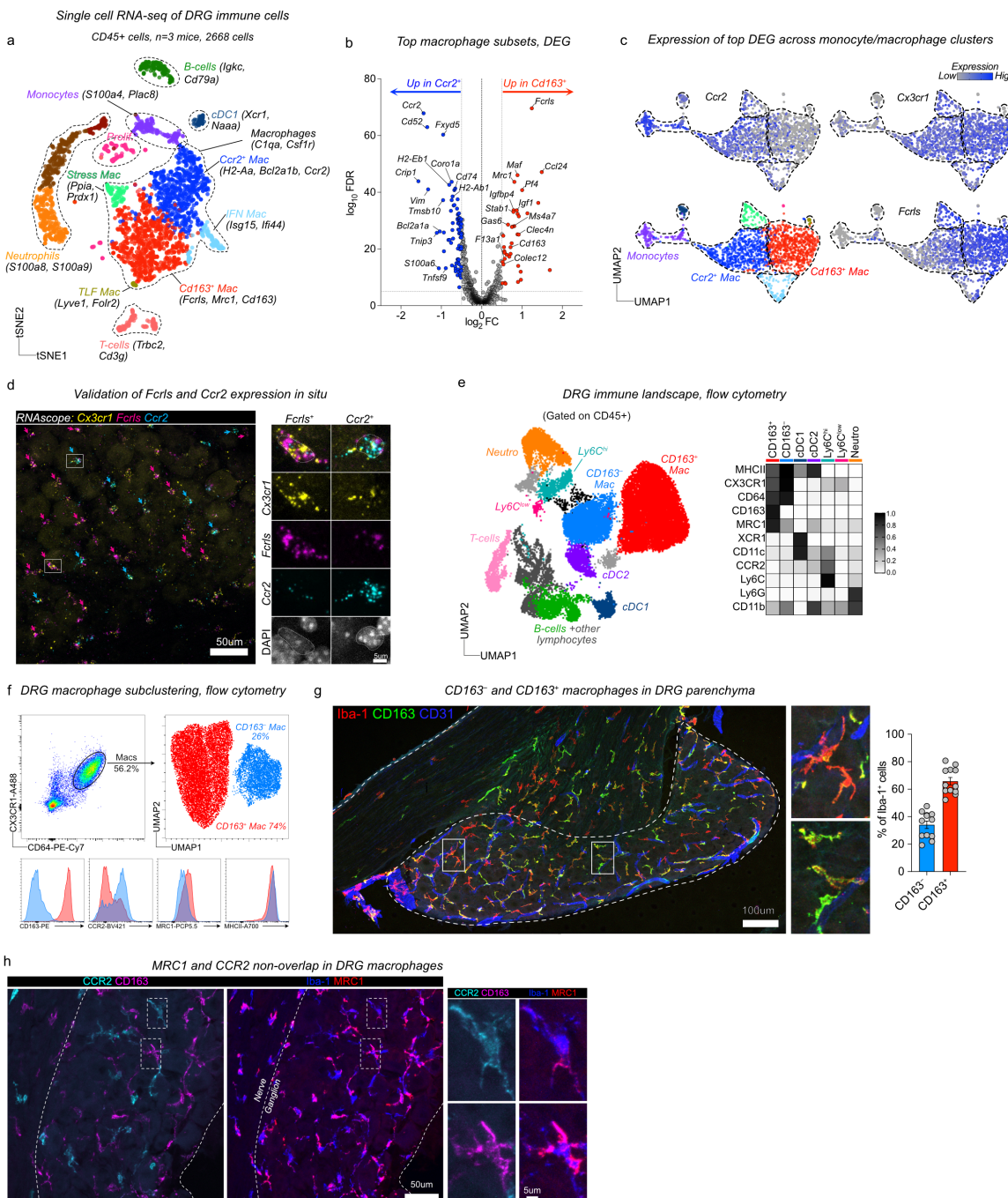
392 We next focused our analysis on the two largest macrophage clusters, as together they made
393 up 87% of the total macrophage pool. Signs of *ex vivo* enzymatic digestion-induced gene
394 expression (Marsh et al., 2022) were apparent, particularly in macrophages (Supplementary
395 Fig. 4a), which included immediate early genes (*Fos*, *Jun*, *Atf3*, *Rhob*). We thus removed
396 these genes after differential gene expression (0.5>log₂FC; log₁₀FDR>5) and before gene
397 ontology analysis. Differential gene expression demonstrated that the largest macrophage
398 cluster (hereafter referred to as CD163⁺ macrophages) highly expressed *Fcrls*, encoding an Fc
399 receptor-like glycoprotein with unknown function, as well as several phagocytic receptors
400 including *Cd163*, *Mrc1* and *Colec12* (Fig. 4b). Consistently, gene ontology analysis showed
401 enrichment of receptor-mediated endocytosis (Supplementary Table 2). *Maf* was also highly
402 expressed in CD163⁺ macrophages, which is a transcription factor essential for perivascular
403 macrophage survival and function (Silva et al., 2021). *F13a1*, *Pf4* and *Selenop*, which are all
404 serum factors were also upregulated in CD163⁺ macrophages, again indicating an interaction
405 with the blood. Consistently, platelet degranulation and regulated exocytosis were additional
406 GO-terms associated with CD163⁺ macrophages (Supplementary Table 2). In addition,
407 CD163⁺ macrophages expressed several chemokines (*Ccl7*, *Ccl8*, *Ccl12*, *Ccl24*, *Pf4*),
408 resulting in enrichment of multiple terms related to chemotaxis (Supplementary Table 2). The
409 second cluster (hereafter referred to as CD163⁻ macrophages) specifically expressed *Ccr2*
410 (Fig 4b-c), a chemokine receptor required for monocyte migration out of the bone marrow
411 (Serbina and Pamer, 2006). Furthermore, *Ccr2* was recently identified as a marker of tissue
412 macrophages that are constantly replaced by circulating monocytes (Dick et al., 2022). 29
413 ribosomal genes were expressed in this subset, resulting in enrichment of several GO-terms
414 related to protein translation (Supplementary Table 3). After removal of ribosomal genes,
415 GO-terms related to neutrophil functions were enriched (*Lgals3*, *Adgre5*, *Anxa2*, *Tlr2*), as
416 well as mononuclear cell migration and type 2 immune responses (*Lgals3*, *Tnf*, *Tnfsf9* and
417 *Cd74*) (Supplementary Table 4). Furthermore, several MHCII genes (*H2-Aa*, *H2-Ab1*, *H2-*
418 *Eb1*, *H2-DMb1*, *Cd74*) were upregulated in CD163⁻ macrophages.

419

420 We then attempted to validate *in situ* expression of the top two differentially expressed genes
421 (*Fcrls* and *Ccr2*, Fig. 4b-c). Using RNAscope, we confirmed expression of *Fcrls* and *Ccr2* in

422 separate subsets of *Cx3cr1*⁺ macrophages, which were both located in the DRG parenchyma,
 423 interspersed between neuronal cell bodies (Fig. 4d). In further support of a parenchymal
 424 location, we did not detect expression of genes enriched in epineurial sciatic nerve
 425 macrophages (*Retnla*, *Cd209a*, *Clec10a*, *Folr2*) (Ydens et al., 2020; Yim et al., 2022) in
 426 either of the two DRG macrophage subsets. In fact, several of these genes were highly
 427 expressed in the TLF macrophage subset, indicating that this population may in fact
 428 correspond to epineurial macrophages (Supplementary Fig. 4b).

429
 430



431
 432 **Figure 4: DRG contains two molecularly distinct macrophage populations**

433 (a) Single-cell RNA-seq analysis of 2668 CD45⁺ DRG cells n= 3 mice. (b) Differential gene expression between CD163⁻ and
 434 CD163⁺ macrophages using the Venice algorithm. (c) UMAP of monocyte/macrophage/cDC clusters and their expression of
 435 key transcripts. (d) RNAscope of indicated transcripts in DRG sections. Purple arrows indicate *Fcrls*⁺*Ccr2*⁻ cells and
 436 turquoise arrows indicate *Fcrls*⁻*Ccr2*⁺ cells. Images are representative of n=3 mice. (e) UMAP of Live, CD45⁺ DRG cells

437 analyzed by flow cytometry. Expression heatmap of selected markers in all myeloid populations. n=4 mice pooled. The
438 experiment was performed three times with similar results. (f) Subclustering of CD64⁺CX3CR1⁺ macrophages from flow
439 cytometry data. (g) Immunostaining and quantification of CD163⁻ and CD163⁺ macrophages in DRG parenchyma. n=12
440 mice. (h) Immunostaining of MRC1 and CCR2 in CD163⁻ and CD163⁺ macrophages.

441

442

443 We next designed a flow cytometry panel to analyze the DRG myeloid landscape in greater
444 detail. We used dimensionality reduction (UMAP) and unbiased clustering (Phenograph)
445 based on 16 parameters (14 surface antigens, size and granularity) combined with traditional
446 gating (Gating strategy in Supplementary Fig. 4c), and this revealed a similar distribution of
447 macrophages, neutrophils, DCs, monocytes and lymphocytes as for our scRNA-seq data (Fig.
448 4e, Supplementary Fig. 4d). To investigate macrophage substructure our panel included
449 several pan-macrophage markers (CD11b, CX3CR1, CD64), as well as potential subset-
450 specific antibodies based on our scRNA-seq data (CD163, CCR2, MRC1 and MHCII). We
451 visualized the DRG macrophage pool (CX3CR1⁺CD64⁺) separately, which assigned all
452 macrophages into two major clusters in the resulting UMAP, defined as CD163⁺CCR2^{low} and
453 CD163⁻CCR2^{hi} (Fig. 4f). MRC1 and MHCII expression provided additional separation
454 between these subsets and were more highly expressed by CD163⁺ and CD163⁻ macrophages,
455 respectively, which was consistent with our scRNAseq data (Fig. 4f). We next turned to
456 immunohistochemistry and confirmed the presence of CD163⁻Iba1⁺ and CD163⁺Iba1⁺
457 macrophages with similar frequencies as our flow cytometry data in the DRG tissue
458 parenchyma (Fig. 4g). Consistent with our flow cytometry data we found that when CCR2
459 and MRC1 antibodies were applied to DRG sections they specifically labeled CD163⁻ and
460 CD163⁺ macrophages, respectively (Fig. 4h). In summary, using scRNA-seq, multi-parameter
461 flow cytometry and immunostaining we identified two distinct macrophage subsets in the
462 DRG, best defined by their differential expression of CD163.

463

464 **CD163⁻ and CD163⁺ macrophages have distinct life cycles**

465 Replenishment of tissue-resident macrophages by circulating monocytes is known to vary
466 across and within tissues (Ginhoux and Guilliams, 2016), shaping macrophage phenotype and
467 function (Blériot et al., 2020). High expression of *Ccr2* was recently identified in a
468 subpopulation of tissue-resident macrophages across several organs that have a high turnover
469 rate from circulating monocytes (Dick et al., 2022). We thus hypothesized that monocytes
470 differentially contribute to the two identified DRG macrophage subsets during steady state,
471 which could have implications on macrophage function. To gain further insight into the
472 relationship between monocytes and CD163⁻ and CD163⁺ macrophages, we removed all
473 lymphocyte, neutrophil and DC clusters from our flow cytometry data and only reclustered
474 cells expressing monocyte or macrophage markers. In the resulting UMAP, Ly6C^{hi} monocytes
475 and CD163⁻ macrophages clustered closely and a new cluster of cells expressing intermediate
476 levels of both monocyte and macrophage markers occupied the space in between (Fig. 5a,
477 referred to as ‘transitioning macrophages’). Ly6C and CCR2 downregulation as well as
478 MHCII, CX3CR1 and CD64 upregulation characterized this transition (Fig. 5b-c), which is
479 consistent with the surface expression changes occurring in ‘monocyte-to-macrophage’
480 conversion in the intestine (Tamoutounour et al., 2012; Bain et al., 2014). *Ear2* and *Retnla*
481 were recently identified as early genes upregulated in monocytes that have recently infiltrated
482 tissues and are committed to a macrophage fate (Sanin et al., 2022). Consistent with our flow
483 cytometry data, we recorded expression of *Ear2* and *Retnla* in cells situated at the border of
484 the CD163⁻ macrophage and monocyte clusters in the scRNA-seq UMAP (Fig. 5d). In DRG
485 tissue sections, CCR2⁺ cells with monocyte morphology were predominantly situated around
486 the capsule and large veins/venules, suggesting monocyte infiltration and differentiation into
487 CD163⁻CD64⁺CCR2⁺ macrophages occurring at this location (Fig. 5e). Taken together, our

488 flow cytometry and scRNA-seq data indicated that Ly6C^{hi} monocytes replenish CD163⁻
489 macrophages, while their contribution to CD163⁺ macrophages appears to be limited.
490

491 To address experimentally if circulating monocytes differentially contributed to CD163⁻ and
492 CD163⁺ macrophage populations, we turned to bone marrow chimeras. We first lethally
493 irradiated CD45.2 mice and reconstituted them with CD45.1 bone marrow. Analysis of
494 chimerism 12 weeks later revealed complete replacement of circulating Ly6C^{hi} monocytes as
495 well as splenic and liver macrophages (Fig. 5f). Conversely, microglia only displayed 13%
496 replacement by monocyte-derived macrophages, consistent with the well-described radio-
497 resistance of microglia and our own previous data (Lund et al., 2018). In the DRG, CD163⁻
498 macrophages were completely replaced by monocyte-derived cells and while a majority of
499 CD163⁺ were also donor-derived, 33% remained of host origin (Fig. 5f). This experiment
500 demonstrates that while Ly6C^{hi} monocytes are able to generate both CD163⁻ and CD163⁺
501 DRG macrophages, CD163⁺ macrophages display partial radio-resistance.
502

503 To avoid the macrophage death and tissue inflammation that accompanies whole-body
504 irradiation, we next set up tissue-protected chimeras. We irradiated only the hindlegs of
505 CD45.2 mice and reconstituted them with CD45.1:*Cx3cr1*^{GFP/+} bone marrow (Fig. 5g,
506 Supplementary Fig. 5a), which after 4 weeks resulted in approximately 30% donor chimerism
507 in the blood. We subsequently analyzed macrophage chimerism in the brain and DRGs over
508 several time points up to 26 weeks after irradiation. In contrast to our whole-body chimeras,
509 microglia now remained completely host-derived throughout the study period (Fig. 5g). We
510 next turned to analyzing DRGs, and observed that over time Ly6C^{hi} monocytes differentially
511 contributed to both CD163⁻ and CD163⁺ macrophages: At 4 weeks, CD163⁻ macrophages
512 were 12.1% donor-derived, a number that rose to 42.0% after 13 weeks and 65.1% after 27
513 weeks (Fig. 5g). For CD163⁺ macrophages these numbers were 2.2% at 4 weeks, 5.7% at 13
514 weeks and 18.0% at 27 weeks (Fig. 5g). In a parallel set of animals we used flow cytometry
515 on pooled DRGs to confirm the findings at the last time point (Supplementary Fig. 5b).
516

517 To validate our results in a setting without irradiation, we made use of *Cx3cr1*^{CreER/+}*R26*^{EYFP/+}
518 mice, in which *Cx3cr1* expressing macrophages can be labeled by the administration of
519 tamoxifen. 72 hours after our tamoxifen regimen, on average 85.9% of microglia were YFP⁺,
520 a number that had not changed after 12 weeks (87.6%) (Fig. 5h), which supports the well-
521 described self-sustainability of microglia (Ajami et al., 2007; Ginhoux et al., 2010; Schulz et
522 al., 2012; Hashimoto et al., 2013). Circulating Ly6C^{hi} monocytes displayed negligible
523 labeling at 72 hours and 12 weeks. In the DRG, CD163⁻ and CD163⁺ macrophages displayed
524 equal labeling 72 hours after tamoxifen (61.1 % vs 65.7 % YFP⁺, respectively). 12 weeks
525 later, while CD163⁺ macrophages retained a similar level of YFP expression (60.2%),
526 CD163⁻ macrophages had dropped to 28.5% YFP⁺ (Fig. 5h). Taken together, our data
527 demonstrate that while CD163⁻ macrophages are constantly replenished from circulating
528 monocytes, CD163⁺ macrophages are mostly self-sustained.
529
530

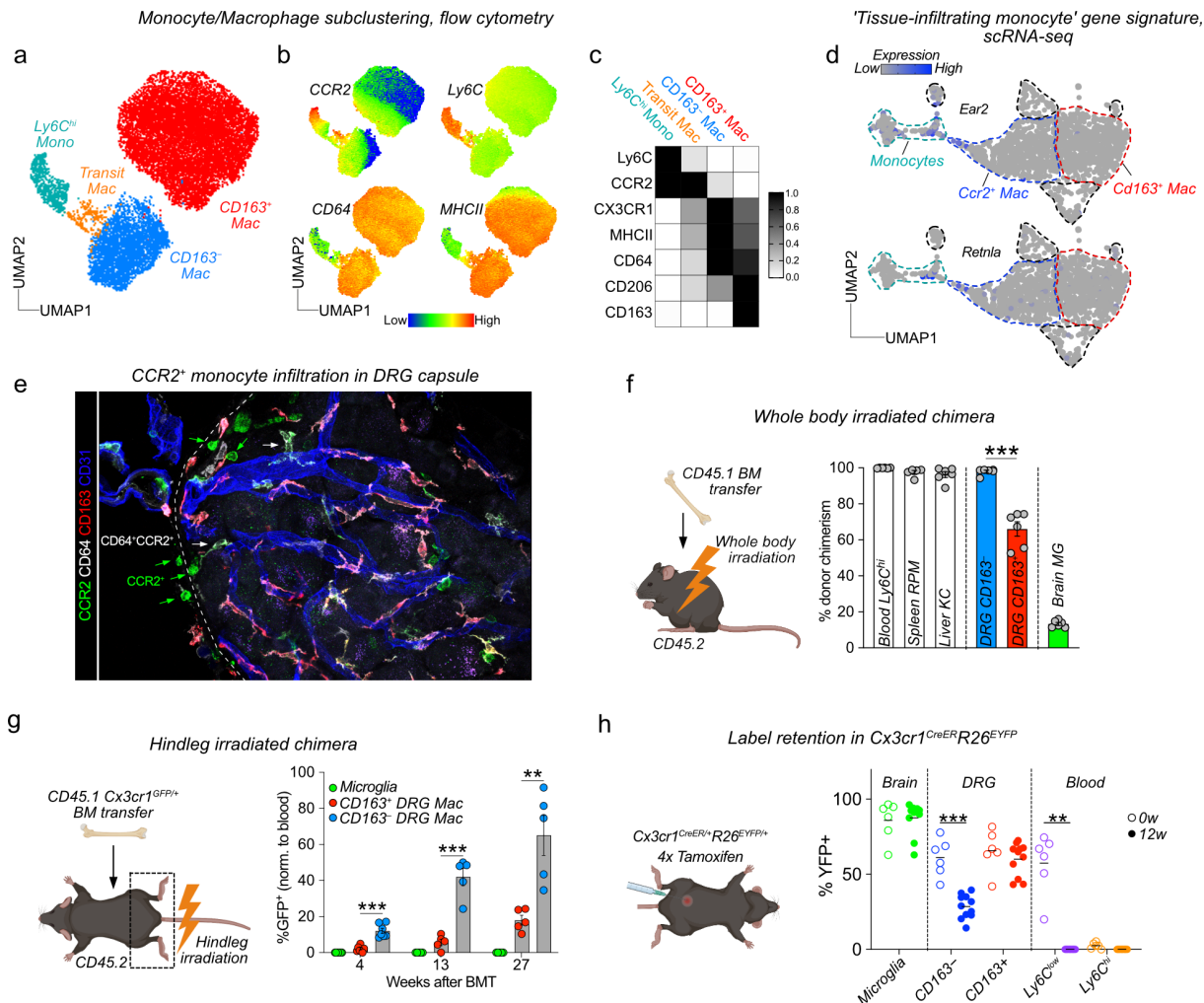


Figure 5: The two DRG macrophage subsets display different turnover by monocytes

(a) Subclustering of DRG monocyte/macrophage clusters in Fig 4e. n=4 mice pooled. (b) Expression of indicated markers across clusters in (a). (c) Heat map with mean marker expression values for indicated populations. (d) Expression of *Retnla* and *Ear2* (genes expressed in recently infiltrated monocytes, Sanin et al 2022) within monocyte/macrophage clusters. (e) Immunolocalization of CCR2⁺ monocytes and CD64⁺CCR2⁺ macrophages adjacent to the DRG capsule (f) Whole body irradiated BM chimera analyzed 12 weeks after irradiation. Frequency of indicated cell populations that are of donor origin, analyzed by flow cytometry. n=6 mice, 1 experiment. Student's unpaired t-test. (g) CD45.2 mice received hindleg irradiation and given an intravenously injected with 5×10^6 bone marrow cells from CD45.1: *Cx3cr1*^{GFP/+} mice. Donor chimerism was assessed by analyzing GFP⁺ cells using immunostaining in tissue sections. n=7, 5, 5 mice. 1 experiment/time point. Tukey's multiple comparisons test. Multiple unpaired t-tests with Holm-Sidak correction. (h) *Cx3cr1*^{CreER/+}/*R26*^{EYFP/+} mice were given 4x2mg tamoxifen injections i.p. and YFP⁺ cells analyzed in indicated cell populations using flow cytometry after 72h (0w) or 12 weeks. (n=6, 11 mice). 2 experiments pooled. Sidak's multiple comparisons test.

Only CD163⁺ macrophages monitor the vasculature

We next assessed functional differences between the two DRG macrophage subsets. Given that the CD163⁺ macrophages expressed several scavenger receptors and displayed a transcriptional signature associated with endocytosis and interaction with the vasculature, we assessed whether the vasculature monitoring function varied between CD163⁻ and CD163⁺ subsets. We first injected fluorescent BSA and analyzed uptake across several organs using flow cytometry. Consistent with our previous analysis of uptake in tissue sections, we found that macrophages in the DRG phagocytosed significantly more BSA than did their ScN or brain counterparts (Fig. 6a). When CD163⁻ and CD163⁺ macrophages were directly compared, uptake was higher in CD163⁺ macrophages (8 fold in the DRG), a finding that was also observed in ScN and the brain (Fig. 6a). We further confirmed a higher phagocytosis of

558 i.v-injected BSA and IgG in CD163⁺ macrophages using DRG tissue sections (Fig. 6b), which
559 additionally allowed us to distinguish macrophages based on their contact with the
560 vasculature. This demonstrated that both CD163 expression (CD163⁻ vs CD163⁺) and
561 macrophage contact with the vasculature (perivascular vs parenchymal) determined the level
562 of BSA and IgG uptake (Fig. 6b). Focusing on perivascular CD163⁻ and CD163⁺
563 macrophages, we next performed spatial mapping of macrophage uptake along the
564 arteriovenous axis. Just as we had observed previously, we found that uptake of all tracers
565 peaked in either v-cap or vein-associated macrophages for both subsets (Fig. 6b).
566 Furthermore, this uptake was significantly higher in CD163⁺ compared to CD163⁻
567 macrophages throughout the arteriovenous axis (Fig. 6b). Taken together, our data
568 demonstrate that *in vivo* monitoring of the vasculature is a function restricted to CD163⁺
569 macrophages.
570

571 **Peripheral inflammation drives arteriovenously zonated activation of endothelium and**
572 **CD163⁺ macrophages**

573 To further explore macrophage-vasculature interplay in the DRG we next assessed the impact
574 of peripheral inflammation on endothelial cells and macrophages. We injected control or
575 macrophage-depleted mice with LPS or saline and sacrificed them after 48h (Fig. 6c). To
576 measure endothelial activation following LPS injection we performed ICAM1 staining, which
577 demonstrated an arteriovenously zonated expression in all experimental groups. In saline-
578 injected mice, ICAM1 could only be detected in veins. After LPS, ICAM1 staining increased
579 across all vessel segments (Fig. 6d). Macrophages were not required for endothelial
580 activation, as mice fed PLX3397 prior to LPS displayed similar upregulation of ICAM1. We
581 next assessed macrophage contact with the vasculature and recorded that endothelial
582 activation was accompanied by increased coverage of the vasculature by macrophages (Fig.
583 6e). Mapping of macrophages along the vasculature demonstrated that endothelial coverage
584 was also arteriovenously zonated, peaking in capillaries and that this was largely driven by
585 increased contact with CD163⁺ macrophages (Fig. 6e). These results demonstrate that
586 peripheral inflammation drives zonated activation of both the endothelium and of CD163⁺
587 macrophages.
588

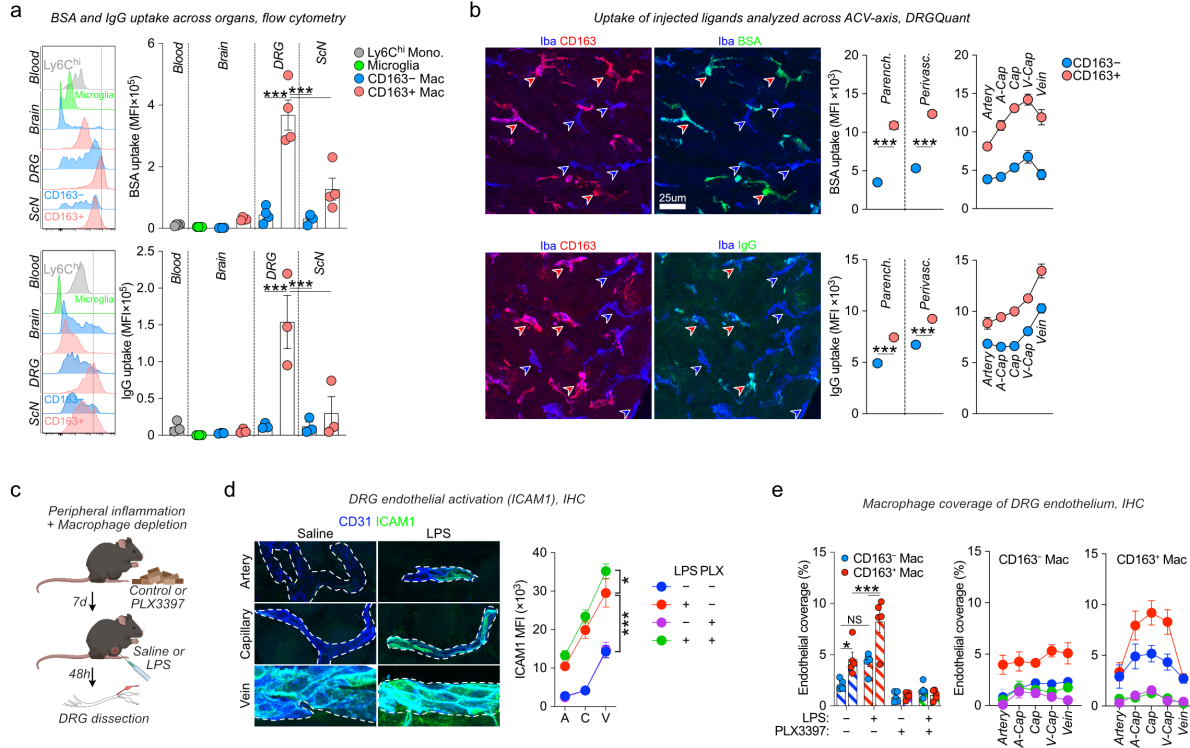


Figure 6: CD163⁺ macrophages interact functionally with the DRG vasculature

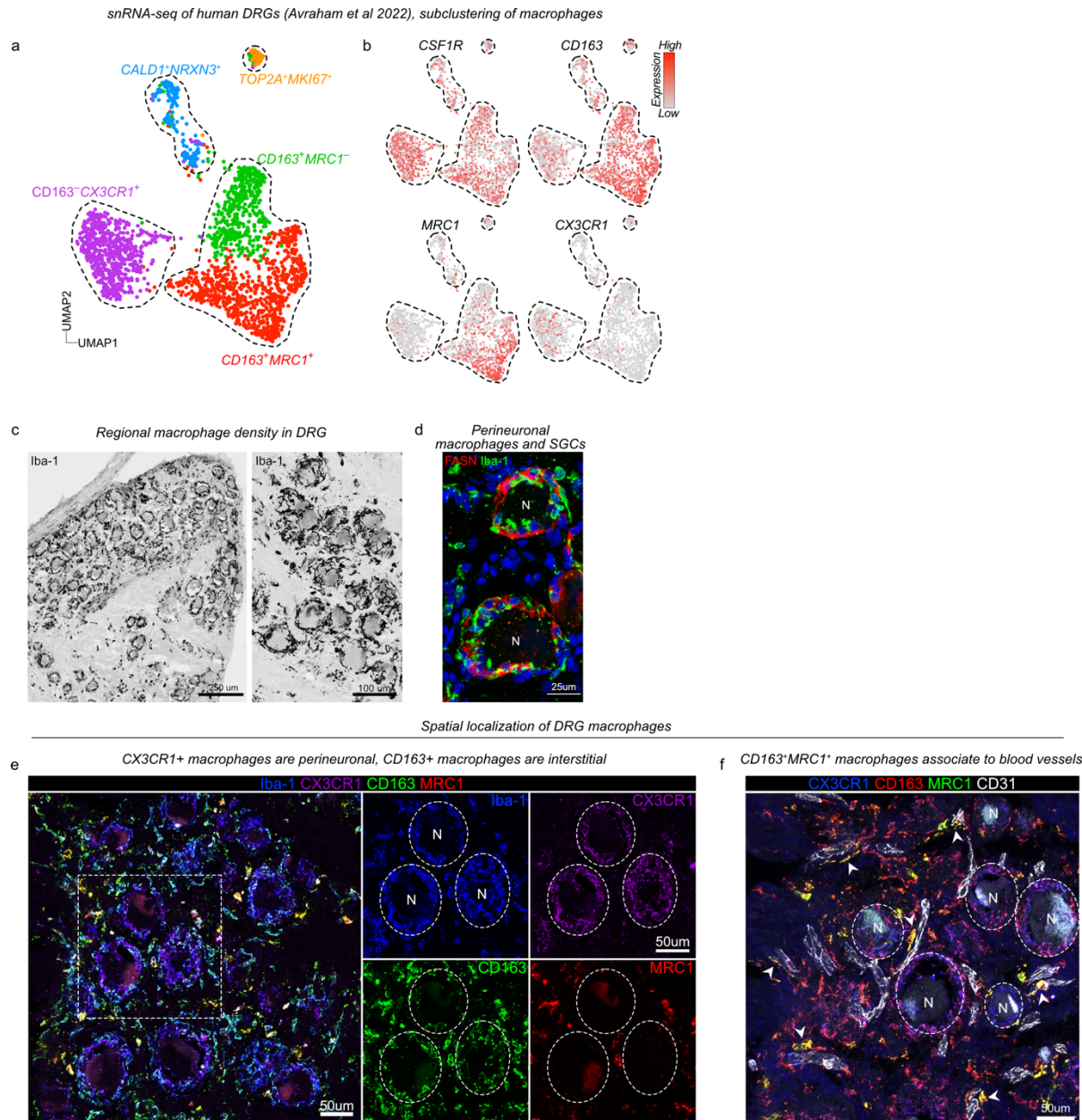
(a) Flow cytometry quantifications of uptake of BSA-A647 (4mg/kg, 1.5h) and IgG-A647 (6mg/kg, 2h) in the indicated organs/cell types. Gated on CD11b⁺Ly6C^{hi} (monocytes), CX3CR1^{hi}CD64^{low} (microglia), CX3CR1⁺CD64^{hi} (macrophages). The experiment was performed twice (IgG, n=5 total) or three times (BSA, n=8 total) with similar results. Tukey's multiple comparisons test. (b) Machine learning (DRGQuant) based analysis of uptake of BSA-A647 (5mg/kg, 1h), goat anti rabbit IgG-A488 (4mg/kg, 4h), 70kDa dextran-TMR (25mg/kg, 1h) in CD163⁻Iba1⁺ and CD163⁺Iba1⁺ macrophages without (parenchymal) or with (perivascular) contact with vasculature. Perivascular macrophages were additionally analyzed based on which vessel segment they contacted. Student's unpaired t-test. (c) Experiment illustration for macrophage depletion and peripheral endotoxin challenge. Mice were fed chow containing 290 ppm PLX3397 and injected i.p. with 1mg/kg LPS. (d) Quantification of ICAM1 expression in CD31⁺ vessel segments. 2-way ANOVA with Tukey's multiple comparisons test. (e) Quantification of endothelial coverage in DRG sections stained with CD31, Iba-1 and CD163.

Perivascular CD163⁺ macrophages are conserved in human DRGs

We next addressed whether CD163⁻ and CD163⁺ macrophages were also present in human DRGs. We again made use of a recently published snRNA-seq dataset of human DRGs (Avraham et al., 2022), which contained 2098 macrophages (clusters expressing *CSF1R*). To investigate macrophage substructure we clustered only macrophages, resulting in 5 distinct clusters (Fig 7a). The largest cluster comprised 38.0 % of all macrophages and was characterized by expression of *CD163*, *MRC1*, *FXIIIa*, *STAB1* and *COLEC12* (Fig. 7b), thus displaying considerable overlap in gene expression with the CD163⁺ macrophage population identified in mouse DRGs. Gene ontology analysis revealed enrichment of biological processes such as receptor mediated endocytosis (*CD163*, *COLEC12*, *TFRC*, *MRC1*, *STAB1*), endothelial tube morphogenesis (*STARD13*, *RBPJ*) and iron/heme metabolism (*HMOX1*, *FXIIIa*, *FTL*, *BLVRB*) (Supplementary Table 5), indicating that this subset (*CD163⁺MRC1⁺*), had a function related to the vasculature, just as we had observed in the mouse. An additional cluster (*CD163⁺MRC1⁻*) accounting for 21.2% of macrophages also expressed *CD163* but lacked most of the defining markers of the *CD163⁺MRC1⁺* macrophages, including *FXIIIa*, *COLEC12* and *MRC1*. No genes were specifically upregulated in this cluster. A third cluster accounted for 29.6 % of macrophages and expressed *C3*, *OXR1* and *KCNIP1* highly, but lacked *CD163*. Differential gene expression also identified *CX3CR1* as a defining marker for

622 this subset ($CD163^-CX3CR1^+$). While this subset displayed similar frequency as $CD163^-$
623 macrophages in the mouse, it did not overlap in gene expression profile. In addition, two
624 smaller clusters expressing markers related to regulation of neuronal function
625 ($CALD1^+NRXN3^+$, 8.7%) as well as proliferation ($TOP2A^+MKI67^+$, 2.5%) were also evident
626 (Fig. 7a-b). $CD163^+$ macrophages are thus conserved in human DRGs and display similar
627 gene expression profiles and putative function.
628

629 In order to validate the presence of the major identified macrophage subsets in human tissues,
630 we again turned to DRG sections from human organ donors (Supplementary Table 1). We
631 first used the pan-macrophage marker Iba-1, which as in the mouse revealed a much higher
632 accumulation of macrophages in the neuronal soma-rich region of DRGs compared to the
633 nerve-rich region (Fig. 7c). In the neuronal soma-rich region macrophages formed dense
634 aggregates around the neuronal cell bodies, but were distinct from $FASN^+$ SGCs (Fig. 7d),
635 which also inhabit this space. In addition, macrophages populated the interstitial space,
636 between the neuronal cell bodies. We next applied subset-specific antibodies to DRG sections
637 and observed that $CX3CR1$ expression was virtually restricted to macrophages surrounding
638 the neuronal soma (Fig. 7e). Conversely, we found that $CD163^+MRC1^+$ and $CD163^+MRC1^-$
639 macrophages were preferentially located in the interstitium than perineuronally (Fig. 7e). Co-
640 staining of $CD31^+$ endothelial cells further revealed that $CD163^+MRC1^+$ were preferentially
641 localized in close contact with endothelial cells (Fig. 7f). In summary, we identify
642 $CD163^-CX3CR1^+$ neuron-associated macrophages which display limited transcriptional and
643 spatial overlap with mouse DRG macrophage subsets. By contrast $CD163^+MRC1^+$
644 macrophages are transcriptionally and anatomically conserved in human DRGs.
645
646



666 astrocytes and pericytes (Zhao et al., 2015). The BNB shares several but not all of these
667 features (Malong et al., 2023), and is recognized as the second most restrictive vascular
668 system in the body (Ubogu, 2020). The DRG is highly vascularized, likely as a consequence
669 of the high metabolic demands of DRG sensory neurons. Consistently, DRG neurons and
670 SGCs produce VEGF during development, which is required for proper vascularization of the
671 DRG (Kutcher et al., 2004). In contrast to the BBB and BNB, it is well documented that the
672 blood vessels supplying the sensory ganglia are more permeable to circulating molecules than
673 those supplying the axons (Olsson, 1968; Jacobs et al., 1976; Arvidson, 1979; Kobayashi and
674 Yoshizawa, 2002). However, a cohesive mechanism for this phenomenon has been lacking.
675 We thus undertook a thorough molecular, structural and spatial characterization of the DRG
676 endothelium. Furthermore, the abluminal side of the DRG vasculature was covered with
677 macrophages with what appeared to be an indiscriminate phagocytic ability. We therefore
678 also characterized the heterogeneity, turnover and function of DRG macrophages.
679

680 **Mechanism of blood-ganglion permeability**

681 To address DRG endothelial permeability in an unbiased way we explored the transcriptome
682 of endothelial cells at the single cell level using a recently published dataset (Avraham et al.,
683 2020). This revealed an arteriovenously zonated profile, progressively changing from having
684 BBB-like properties (*Cldn5*⁺) to displaying features of peripheral endothelial beds (*Plvap*⁺).
685 CLDN5 participates in barrier integrity at the BBB and blood-retinal barrier by limiting
686 paracellular diffusion between blood and tissue (Greene et al., 2019). Regional differences in
687 tight junction expression, including CLDN5, between neuronal soma and fiber-rich regions in
688 the DRG have been reported (Hirakawa et al., 2004; Lux et al., 2019). We here clarify that
689 this is a consequence of reduced expression of CLDN5 along the arteriovenous axis, which is
690 a feature shared by several peripheral endothelial beds (Richards et al., 2022), but not the
691 brain vasculature (Vanlandewijck et al., 2018; Kalucka et al., 2020). We did not directly
692 assess the contribution of reduced CLDN5 expression to endothelial permeability, but
693 experimental evidence suggests it is mostly important for small molecular weight compounds.
694 CLDN5 mutant mice display increased permeability only to molecules <0.8kDa at the BBB
695 (Nitta et al., 2003). Outside of the CNS, endothelial cell-specific CLDN5 loss does not affect
696 basal permeability to 10-70 kDa dextrans, but increases histamine-induced permeability in an
697 organ-specific manner (Richards et al., 2022).
698

699 Given the high expression of PLVAP in veins we addressed its role in endothelial
700 permeability. PLVAP is restricted to the diaphragm of endothelial fenestrae, transendothelial
701 channels and caveolar vesicles (Stan et al., 1999, 2004). However, the high expression of
702 *Plvap* at mRNA and protein levels in veins and v-caps did not overlap with the absent
703 transendothelial channels and the scarcity of endothelial fenestrae that we observed using
704 TEM and SEM. Several studies have reported endothelial fenestrae in the DRG vasculature
705 (Anzil et al., 1976; Jacobs et al., 1976; Arvidson, 1979; Kobayashi and Yoshizawa, 2002), but
706 their absolute abundance has not been quantified. In venous capillaries, where fenestrae were
707 most abundant, we observed that less than 0.1% of the endothelial lumen was covered with
708 fenestral openings. By comparison, 12.8% of the luminal surface of the glomerular
709 endothelium of the kidney is covered by fenestrae (Bulger et al., 1983). Based on this finding
710 we find it unlikely that endothelial fenestrae contribute significantly to basal permeability of
711 the DRG endothelium. However, we do not exclude that fenestrae serve other critical
712 purposes important for DRG physiology, such as chemosensation of the body's internal
713 milieu, similar to sensory circumventricular organs (Miyata, 2015), as previously proposed
714 (Devor, 1999). The limited number of fenestrae and their specific spatial localization to v-
715 caps would support a tightly regulated mechanism.

716

717 While fenestrae were limited, as much as 10% of the endothelial cytoplasm in v-caps
718 contained caveolar vesicles. It has been proposed that caveolae and fenestrae are
719 interchangeable structures (Satchell and Braet, 2009). However, we excluded this possibility
720 in the DRG endothelium based on the presence of fenestrae in *Cav1* mutant mice.
721 Furthermore, using these mice we functionally validated the importance of caveolar vesicles
722 for basal permeability of the DRG endothelium. Given that *Cav1* mRNA was not
723 arteriovenously zonated, we speculated that caveolar assembly must be regulated post-
724 translationally. This led us to explore the levels of MFSD2A, a transporter of DHA, an
725 essential fatty acid required for proper brain development and function (Nguyen et al., 2014).
726 The transporter activity of MFSD2A creates a lipid environment in endothelial cells that
727 interferes with caveolar assembly at the BBB (Andreone et al., 2017) and blood-retinal barrier
728 (Wang et al., 2020b). MFSD2A expression is only described in the brain, testis and retinal
729 endothelium. While MFSD2A expression was absent in blood vessels supplying the axons of
730 sensory neurons, it was highly and specifically expressed in ganglionic endothelial cells. In
731 the DRG, MFSD2A expression peaked in a-caps and progressively dropped to non-detectable
732 levels in veins, which negatively correlated with CAV1 expression, thus suggesting MFSD2A
733 could be a negative regulator of caveolar transcytosis also in the DRG. Manipulation of
734 MFSD2A expression at the DRG could thus be a viable strategy to alter blood-ganglion
735 permeability.

736

737 Caveolar transcytosis represents a mechanism that could potentially be pharmacologically
738 targeted to reduce DRG endothelial permeability, or alternatively co-opted to deliver drugs
739 into the DRG parenchyma (Kiseleva et al., 2018; Marchetti et al., 2019). This could be
740 desirable in sensory ganglionopathies (Amato and Ropper, 2020), which include
741 paraneoplastic and autoimmune conditions, infections, platinum-based chemotherapy
742 (Dzagnidze et al., 2007; Gupta and Bhaskar, 2016), and likely also fibromyalgia (Goebel et
743 al., 2021; Martínez-Lavín, 2021; Krock et al., 2023).

744

745 In addition to the molecular mechanism of DRG endothelial permeability, our findings led us
746 to conclude that the DRG arteriovenous tree is anatomically organized in a conserved manner:
747 arteries and arterial capillaries at the nerve/ganglion interface, venous capillaries directly
748 underlying the capsule, and veins running along the surface of the DRG. Differences in
749 vascularization (Jimenez-Andrade et al., 2008; Kobayashi et al., 2010), expression of tight
750 junctions (Lux et al., 2019) and endothelial permeability between the fiber-rich area and the
751 neuronal soma-rich area of the DRG have been described (Reinhold and Rittner, 2020). Our
752 data now clarifies that this is a consequence of arteries entering the DRG body from the nerve
753 fibers. The impermeable arteries are always localized in the fiber-rich area. By contrast, the
754 neuronal soma-rich area only contains capillaries and veins. Taken together, our data
755 challenges the assumption that the DRG completely lacks an endothelial barrier (Devor, 1999;
756 Haberberger et al., 2019). We instead propose that the DRG endothelial patterning is highly
757 regulated to create a tight barrier in arteries and arterial capillaries which tapers off toward
758 venous capillaries and veins, providing the neuronal soma and interstitial cells underlying the
759 capsule with a high exposure to circulating macromolecules. In addition, we validate CLDN5
760 and PLVAP as markers of arterial and venous capillaries. This framework can help in the
761 interpretation of future and even previous studies.

762

763 Function of DRG perivascular macrophages

764 After peripheral nerve damage, macrophages accumulate not only at the site of injury but also
765 around axotomized neuronal cell bodies in the DRG (Niemi et al., 2013; Peng et al., 2016;

766 Kalinski et al., 2020), a process that promotes axon regeneration (Kwon et al., 2013; Niemi et
767 al., 2013; Feng et al., 2023) as well as the development of neuropathic pain (Yu et al., 2020).
768 Most studies of DRG macrophages have been guided by this and analogous findings, which
769 has placed a heavy focus on macrophage-sensory neuron crosstalk in the understanding of
770 DRG macrophage biology (Gheorghe et al., 2022). We here propose that an additional critical
771 function of DRG macrophages is to interact with the vasculature. Several of our experiments
772 support this claim: CD163⁺ macrophages displayed a vasculature-associated transcriptional
773 profile, made close contact with endothelial cells, rapidly phagocytosed circulating
774 macromolecules and increased vessel coverage in response to circulating endotoxin.
775

776 CD163⁺ macrophages specifically expressed MRC1 (CD206) at both mRNA and protein
777 levels, which represents a marker that has recently been used to define pain-resolving ‘M2-
778 macrophages’ in DRGs. MRC1⁺ DRG macrophages expand during cisplatin chemotherapy,
779 producing IL-10 that leads to the resolution of pain (Singh et al., 2022). Similarly, in a model
780 of carrageenan-induced hyperalgesia, MRC1⁺ DRG macrophages increase in number and
781 drive pain-resolution by transferring mitochondria to sensory neurons (Vlist et al., 2022). In a
782 model of osteoarthritis pain in which iNOS⁺ macrophages predominate in DRGs and maintain
783 chronic pain, transferring M2-polarized macrophages (expressing MRC1) resolved pain
784 (Raoof et al., 2021). Whether the MRC1⁺ macrophages identified in these reports correspond
785 to the CD163⁺ vasculature-monitoring subset identified in our study remains to be explored. It
786 would also be of particular interest to understand whether these pain-resolving functions are
787 connected with the CD163⁺ macrophage phenotype, and whether it is dependent on contact
788 with or information conveyed through the vasculature.
789

790 The observations that DRG macrophages localized around endothelial cells filled with
791 caveolae, and that macrophage phagocytic ability aligned with peak endothelial permeability,
792 leads to the interpretation that the CD163⁺ macrophage network has developed in order to
793 limit enhanced permeability in the DRG. This function is described for perivascular
794 macrophages in the cochlea (Zhang et al., 2012), skin (He et al., 2016) and more recently in
795 the sciatic nerve (Malong et al., 2023). Depletion of macrophages in all these organs results in
796 vessel hyperpermeability. Similarly, CD163⁺ macrophages located in close proximity to
797 fenestrated blood vessels in the area postrema of the brain sequester blood proteins (Willis et
798 al., 2007). However, we did not observe increased leakage of injected tracers into the DRG
799 parenchyma following macrophage depletion. However, we cannot exclude that the non-
800 depleted macrophages (10%) were capable of phagocytosing the injected tracers in the time
801 frame we used in our study (3 hours).
802

803 In an effort to link the ontogeny of the DRG macrophage subsets to their phenotype and
804 function (Blériot et al., 2020), we also addressed their turnover from circulating monocytes.
805 This revealed that CD163⁺ macrophages were largely self-sustained, whereas CCR2⁺
806 macrophages were almost completely replaced by monocytes over 27 weeks. In a recent
807 preprint article, parabiosis experiments confirm the presence of donor-derived macrophages
808 in the DRG parenchyma in naive mice (Guimarães et al., 2022). In addition, our findings
809 agree with the ambitious study by Dick *et al*, which identified tissue-resident CCR2⁺
810 macrophages in several organs that were almost completely replaced by circulating
811 monocytes (Dick et al., 2022).
812

813 Finally, when comparing the transcriptional profile of human and mouse DRG macrophages
814 we concluded that only CD163⁺ macrophages displayed a gene signature that was conserved.
815 Taken together with the perivascular localization of CD163⁺ macrophages in human DRGs,

816 we suggest that CD163⁺ macrophages fulfill an important physiological function associated
817 with endothelial monitoring, as they have been conserved for 90 million years of evolution.
818
819

820 Methods

821

822 Mice

823 All mice were either purchased from approved vendors or bred and maintained under specific
824 pathogen-free conditions at Karolinska Institutet, in accordance with national animal care
825 guidelines. All animal experiments were approved by the appropriate ethical review board
826 (Stockholms djurförsöksetiska nämnd). C57BL/6 mice were purchased from Charles River
827 (C57BL/6J) or bred locally (C57BL/6NTac). BALB/cAnNRj mice were purchased from
828 Janvier. The following strains were originally purchased from the Jackson Laboratory and
829 bred locally: CD45.1 (Jax 002014), *Cav1*^{-/-} mice (Jax 007083) (Razani et al., 2001), *Cx3cr1*^{gfp}
830 (Jax 005582, gift from C. Gerlach, Karolinska Institutet) (Jung et al., 2000), *Cx3cr1*^{CreER} (Jax
831 020940) (Yona et al., 2013) and R26R-EYFP (Jax 006148) (Srinivas et al., 2001).
832 *Cldn5*(BAC)-eGFP mice (Laviña et al., 2018) were a gift from C. Betsholtz (Uppsala
833 University).

834

835 In vivo studies:

836 Macrophage depletion using PLX3397:

837 PLX3397 was formulated into A04 standard diet (Safe Nutrition Service, France) at 75ppm or
838 290ppm and was administered *ad libitum* for 7 or 21 consecutive days. Identical diet without
839 PLX3397 was used as control.

840

841 Tamoxifen administration

842 Tamoxifen (T5648, Sigma) was resuspended in corn oil (C8267, Sigma) and administered i.p
843 to *Cx3cr1*^{CreER}*R26*^{EYFP} mice at 1mg/10g body weight, 4 times over a 5 day period.

844

845 Whole-body irradiation chimera

846 CD45.2 mice were irradiated with 9.5 Gray using an X-RAD 320 irradiation source
847 (0.95Gray/minute) with a 20 × 20 cm irradiation field and reconstituted the same day with
848 5×10⁶ CD45.1 BM cells by tail vein injection. Tissue chimerism was analyzed 12 weeks later.

849

850 Hindleg bone marrow chimera

851 Irradiation of only hindlegs was accomplished by maintaining CD45.2 mice under isofluorane
852 anaesthesia and placing the body outside the field of irradiation (the irradiation source is
853 equipped with a lamp to visualize the 20×20 cm irradiation field). Mice were reconstituted the
854 same day with 5×10⁶ BM cells from CD45.1/CD45.2:*Cx3cr1*^{gfp/+} or
855 CD45.1/CD45.1:*Cx3cr1*^{gfp/+} mice by tail vein injection, and analyzed at 4, 13, 26 or 33 weeks.

856

857 Tracer injections

858 Anaesthetic cream was applied to the tail 20 min prior to iv injections. Tracers were injected
859 via the tail vein at 4ul/g body weight. Doses and circulation times are summarized in figure
860 legends for each experiment. The following tracers were used: Goat anti Rabbit IgG-A488
861 (Thermo, A11008), Goat anti Human IgG-A647 (Jackson Immuno, 109-605-003), BSA-A488
862 (Thermo, A13100), BSA-A647 (Thermo, A34785), 3kDa dextran-TMR (Thermo, D3308),
863 70kDa dextran-TMR (Thermo, D1818), 500kDa dextran-FITC (Thermo, D7136), 2000kDa
864 dextran-FITC (Thermo, D7137). Mice were subsequently sacrificed and transcardially
865 perfused with PBS only and immediately dissected (flow cytometry analysis) or PBS

866 followed by 4% formaldehyde (immunohistochemistry analysis) followed by 24h post-
867 fixation in 4% formaldehyde.
868

869 *LPS injections*

870 Mice were injected i.p with LPS (1mg/kg) (Condrex, Serotype 0111:B4) or saline vehicle and
871 sacrificed 48h later.
872

873 **Whole mount and optical clearing**

874 DRG staining and optical clearing were performed according to (Hunt et al., 2022) using a
875 modified version of the iDISCO protocol (Renier et al., 2014). Briefly, DRGs dissected with
876 the dorsal/ventral roots and peripheral nerve attached were washed and permeabilized in PBS
877 and 0.2% Triton X-100 (PTx) for 3 hours, rinsed in PBS and 0.2% Tween-20 (PTw). DRGs
878 were then incubated 72h with primary antibodies diluted in PTw. After thorough washing in
879 PTw, DRGs were incubated 48h with secondary antibodies diluted in PTw protected from
880 light. Finally, DRGs were washed in PTw before tissue clearing. Stainings were performed in
881 0.5ml Eppendorf tubes on a tube rotator. DRGs were either imaged directly (CLDN5-GFP) or
882 optically cleared to improve signal depth. Optical clearing was performed in 50ml glass flasks
883 at room temperature (RT) by first dehydrating DRGs in increasing concentrations of
884 tetrahydrofuran (THF) in distilled water (dH₂O): 50%, 70%; 80%, 2x100% (10 min/solution)
885 followed by refractive index matching in dibenzyl ether (DBE; 2x10min). Cleared tissues
886 were mounted in DBE in custom made 3D-printed image chambers according to (Hunt et al.,
887 2022) and imaged using a confocal microscope.
888

889 **Immunostaining**

890 Standard methods for immunostaining were applied. Tissues were collected from
891 animals perfused with 4% formaldehyde followed by direct dissection and no post-fixation or
892 post-fixation for 24 hours followed by dissection. The different fixation protocols were
893 chosen based on downstream staining protocols. Tissues were embedded in OCT and
894 sectioned using a cryostat at 25-40µm onto SuperFrost Plus glass slides. Sections were stored
895 at -20°C until staining. For stainings, sections were allowed to thaw at RT for 1 hour, washed
896 in PBS for 20 minutes and blocked with 3 % donkey serum in PBS + 0.2% Triton X-100 for
897 30-60 minutes. Tissues were then incubated with primary antibodies (Supplementary Table
898 6), diluted in 0.2% Triton X-100, overnight at 4°C. After 3x10 min washes in PBS, secondary
899 antibodies (Thermo or Jackson ImmunoResearch), diluted in PBS, were applied and sections
900 incubated for 2h at RT. After another round of washing, sections were mounted using
901 ProLong gold (Thermo). If not otherwise stated, 3D-images shown in figures were made
902 using Imaris software, 2D-images presented in figures are maximum intensity projections of
903 acquired z-stacks.
904

905 **RNAscope**

906 RNAscope was performed according to manufacturer's protocol for RNAscope Multiplex
907 Fluorescent Detection Reagents v2 (ACD, 323110). Briefly, slides were washed in 1X PBS
908 for 5 min and baked in the HybEZ Oven for 30 min at 60°C. A 15 min fixation in cold 4%
909 PFA was done prior to dehydration with 50%, 70% and twice 100% ethanol for 5 min at RT.
910 Slides were then dried at RT and H₂O₂ (ACD, 322335) was applied so that the tissue was
911 covered. This incubation was done for 10 min at RT and the slides were washed in MilliQ
912 water. The slides were transferred into a 1X target retrieval solution (ACD, 322000) at 100°C
913 and kept in this solution for 5 min after which they were washed in MilliQ and 100% ethanol.
914 A circle was drawn around the tissue using a ImmEdge Pen (Vector laboratories, H-4000).
915 The slides were left to dry at RT overnight. Protease III (ACD, 322337) was applied for 30

916 min at 40°C in the HybEZ Oven. The slides were washed in MilliQ water and a solution of
917 1X probes was applied for 2 hours at 40°C in the HybEZ Oven. The 1X probe solution was
918 prepared by diluting *Fcrls*-C2 (ACD, 441231-C2) and *Cx3cr1*-C4 (ACD, 314221-C4) 50
919 times in 1X *Ccr2*-O1 (ACD, 501681). The slides were washed using 1X wash buffer (ACD,
920 310091) and the amplification reagents AMP1, AMP2 and AMP3 were applied for 30,30 and
921 15 minutes respectively at 40°C with washes in wash buffer after each incubation. HRP-C1
922 was applied for 15 min at 40°C after which the slides were washed in wash buffer and
923 incubated with Opal dye 570 (Akoya, OP-001003) diluted 1:1500 in TSA buffer (ACD,
924 322809) for 30 min at 40°C. Upon another wash in wash buffer the HRP blocker solution was
925 applied for 15 min at 40°C. The same steps were repeated for HRP-C2 with Opal 690 (Akoya,
926 OP-001006) and HRP-C4 with Opal 520 (Akoya, OP-001001) diluted 1:3000. After the final
927 wash, spectral DAPI was applied to the slides for 30 seconds. The slides were mounted with
928 ProlongGold mounting media.
929

930 **Confocal imaging**

931 Z-stack images were acquired using a Zeiss LSM800 laser-scanning confocal microscope
932 equipped with 4 lasers (405nm, 488nm, 561nm and 640nm)
933

934 **STED**

935 Super-resolution STED imaging was performed using a STEDYCON (Abberior Instruments)
936 equipped with excitation lasers at 488 nm, 561 nm and 640 nm and a STED laser at 775 nm.
937 Deconvolution was performed on all STED images using Huygens software.
938

939 **Transmission electron microscopy (TEM)**

940 Mice were perfused with 2.5 % glutaraldehyde and 1% formaldehyde in 0.1M phosphate
941 buffer, pH 7.4, followed by post-fixation in the same solution (>24h). Following fixation the
942 DRGs were rinsed in 0.1M phosphate buffer prior to post-fixation in 2% osmium tetroxide in
943 0.1M phosphate buffer, pH 7.4 at 4°C for 2 hour. DRGs were then stepwise dehydrated in
944 ethanol followed by acetone and resin embedded in LX-112 (Ladd). Ultrathin sections
945 (approximately 80-100 nm) were prepared using an EM UC 7 (Leica) and contrasted with
946 uranyl acetate followed by lead citrate. The sections were examined using a Hitachi HT7700
947 transmission electron microscope (Hitachi High-Technologies) at 80 kV digital images were
948 acquired using a 2kx2k Vela CCD camera (Olympus Soft Imaging Solutions).
949

950 **Scanning Electron Microscopy (SEM)**

951 Following rinsing in 0.1 M phosphate buffer and MilliQ, DRGs were subjected to stepwise
952 dehydration using ethanol and prior to critical point drying in an EM CPD 030 (Leica). The
953 DRG were finally mounted on aluminium pins using double-sided carbon adhesive tabs and
954 platinum coated using a Q150T ES (Quorum). The DRGs were analysed using an Ultra 55
955 field emission scanning electron microscope (Zeiss) at 3 kV using the SE2 detector.
956

957 **Image analysis (Imaris)**

958 Imaris software was used to quantify marker expression across DRG vessel segments.
959 PLVAP and CLDN5-GFP were quantified in sections stained with CD31 and ACTA2 and
960 vessels assigned as arteries (ACTA2⁺, diameter>10um), capillaries (ACTA2⁻,
961 diameter<10um) or veins (ACTA2⁺ on DRG surface, diameter>10um). The zonated
962 expression of PLVAP and CLDN5 in the DRG vasculature was subsequently utilized to
963 quantify MFSD2A and CAV1 expression (MFI) across vessel segments using the following
964 criteria: Arteries (same as above), a-caps (ACTA2⁻, PLVAP⁻ or CLDN5⁺ diameter<10um),

965 v-caps (ACTA2⁻, PLVAP⁺ or CLDN5⁻, diameter<10um). MFI expression was calculated for
966 each vessel segment and normalized to %max for each animal.
967

968 **Image analysis (DRGQuant)**

969 Images were analyzed using the DRGquant pipeline described previously (Hunt et al., 2022).
970 In brief, UNET (Ronneberger et al., 2015) models were trained to identify vasculature,
971 macrophages, neuronal-rich regions of the DRG, fiber-rich regions of the DRG, endothelial
972 cells (TEM), vascular lumen (TEM). Model outputs were then run through macros in FIJI
973 (Schindelin et al., 2012) that segmented structures in using connected component analysis in
974 CLIJ (Haase et al., 2020). Macrophages identities were classified as follows: DRG
975 macrophage ($\geq 30\%$ volume within the neuronal soma rich region, Fiber macrophage (Non-
976 DRG macrophage with $\geq 30\%$ volume in fiber-rich region), parenchymal macrophage (surface
977 area of less than $10\mu\text{m}^2$ in contact with blood vessels), perivascular macrophage (surface area
978 greater than $10\mu\text{m}^2$ in contact with blood vessels). A FIJI macro was written for semi-
979 automated segmentation of the arteriovenous axis with the following workflow: 2D
980 projections of vascular/endothelial cell markers were annotated by an expert as vein, v-cap,
981 capillary, a-cap or artery. Annotations were converted into 2D masks which were then applied
982 to the 3D vasculature map identified via UNET. Perivascular macrophages were then
983 classified based on the vessel type they were most closely associated with. Macrophage
984 morphology as well as fluorescent intensities were quantified using ImageJ's 3D ROI
985 manager (Ollion et al., 2013). A script was written in python that concatenated all data tables
986 generated in FIJI. For identification of endothelial vesicles (caveolae) in TEM images a
987 stardist (Schmidt et al., 2018) model was trained. A Fiji macro was written that used the
988 UNET output in combination with the stardist output to isolate only vesicles present in the
989 endothelial cells. Single vesicles were defined by a diameter of <100nm and fused vesicles
990 were defined by a diameter greater than 100nm. For all datasets a summary image
991 highlighting all classified objects was generated and visually inspected to ensure the quality
992 of the analysis.
993

994 **Generation of single cell suspensions**

995 Mice were euthanized with pentobarbital (APL, 338327) overdose i.p. When applicable,
996 blood was collected from the right ventricle prior to perfusion into an EDTA- or Heparin-
997 coated syringe. Mice were perfused with ice- cold PBS and neural tissues dissected into cold
998 PBS. For analysis by flow cytometry a 5mm coronal slice of the right forebrain was used,
999 both sciatic nerves and approximately 40 pooled cervical, thoracic and lumbar DRGs. Neural
1000 tissues were digested in 2mg/ml Collagenase I (Gibco 17100-017), 5mg/ml Dispase II
1001 (Sigma, D4693) and 0.5mg/ml DNase I (Roche, 11284932001) at 37C for 30min (Brain) or
1002 40min (DRGs and ScN). Myelin was removed using 38% Percoll (Sigma, GE17-0891-02)
1003 and the cells were subsequently washed and resuspended in PBS. 200 μl blood was lysed in
1004 ACK-buffer (Gibco, A1049201) and centrifuged. The pellet was resuspended in PBS and
1005 used for staining.
1006

1007 **Flow cytometry**

1008 Flow cytometry data was acquired using a Cytokem Aurora equipped with violet (405nm), blue
1009 (488nm) and red (640nm) lasers. The following antibodies and stains were used: CCR2-
1010 BV421 (clone 475301, BD, 747963), Ly6C-BV510 (clone HK1.4, Biolegend, 128033), B220-
1011 BV605 (clone RA3-6B2, Biolegend, 103243), Ly6G-BV711 (clone 1A8, Biolegend, 127643),
1012 CD11c-BV785 (clone N418, Biolegend, 117336), CX3CR1-A488 (clone SA011F11,
1013 Biolegend, 149021), CX3CR1-BV785 (clone SA011F11, Biolegend, 149029), CD163-PE
1014 (clone TNKUPJ, Thermo, 12-1631-80), CD64-PE/Cy7 (clone X54-5/7.1, Biolegend, 139313),

1015 MRC1-PCP5.5 (clone C068C2, Biolegend, 141716), CD11b-PEFire640 (clone M1/70,
1016 Biolegend, 101279) TCRb-APC (clone H57-597, Biolegend, 109212), MHCII-A700 (clone
1017 M5/114.15.2, Biolegend, 107622), XCR1-APC/Cy7(clone ZET, Biolegend, 148223), CD45-
1018 APC-Fire810 (clone 30F11, Biolegend 103173) CD45.1-A647 (clone A20, Biolegend,
1019 110720), CD45.2- BV785 (clone 104, Biolegend, 109839), LIVE/DEAD Violet dead cell
1020 stain kit (Thermo, L34955). Flow cytometry data was analyzed using Flowjo 10 software.
1021 Dimensionality reduction and cluster identification was performed using the UMAP and
1022 Phenograph packages, respectively.
1023

1024 **Single cell-RNA-seq**

1025 Single cell suspensions of DRG cells from BALB/cAnNRj mice were blocked with FcR
1026 blocking solution (Miltenyi Biotec 1 No.130-092-575) and stained with anti-CD45:PE
1027 (BioLegend 103105). Additionally, TotalSeq™ anti-mouse Hashtag antibodies were used to
1028 label individual samples (BioLegend 155803, 155805, 155809). The samples were strained
1029 through a 35-micron filter. DAPI was added to the cell solution in order to exclude dead cells.
1030 CD45⁺DAPI⁻ cells were sorted on a BD Influx sorter. The sorted cells were pooled into a
1031 single lane on the 10x Genomics Chromium Single Cell 3' v3 system. Library preparation
1032 and sequencing were performed at the SciLifeLab sequencing facility, Solna using an
1033 Illumina HiSeq 2500 at 61,006 reads/cell. The 10X CellRanger output files (barcodes, feature
1034 and count matrix) were analyzed using Seurat in R studio. The filtering criteria was set to
1035 include cells with more than 200 and less than 5000 genes as well as less than 5%
1036 mitochondrial reads. The data was normalized and scaled using the Seurat functions
1037 (NormalizeData and ScalaData). The three samples were demultiplexed using the
1038 HTDemux function. Variable features were found using the *vst* method in the
1039 FindVariableFeatures function with nfeatures set to 2000 and were used to compute the PCAs
1040 using RunPCA. K-nearest and shared nearest neighbor analysis were computed using
1041 FindNeighbors with 15 dimensions. Graph-based clustering was conducted using the Louvain
1042 algorithm in the FindClusters function with the resolution set at 0.5 (informed by clustertree
1043 produced by Clustree). RunUMAP was used to visualize the clusters. Annotation was done
1044 using the SingleR package to compare transcriptomes in the ImmunoGen database and based
1045 on known cell type markers. For visualization and differential gene expression analysis, data
1046 was exported to Bioturing Browser 3.
1047

1048 **Endothelial cell enrichment and qPCR**

1049 Single cell suspensions were prepared from liver, lung, kidney, brain and DRGs by enzymatic
1050 digestion at 37°C using the following enzymes and incubation times. Liver, small piece of
1051 one lobe (1mg/ml Collagenase I Gibco 17100-017, 1mg/ml Collagenase II Worthington
1052 LS004176, 5mg/ml Dispase II Sigma D4693 and 7.5ug/ml DNase I Roche 11284932001,
1053 30min) Lung, one lobe (1mg/ml Collagenase II, 2.5mg/ml Collagenase IV Worthington
1054 LS004188 and 15ug/ml DNase I, 50 min). Kidney, one (2mg/ml Collagenase I and 7.5ug/ml
1055 DNase I, 45min), Forebrain (2mg/ml Collagenase I, 0.5mg/ml DNase I, 30min) and DRGs,
1056 approx. 40 (2mg/ml Collagenase I, 5mg/ml Dispase II, 0.5mg/ml DNase I, 45min). Single
1057 cell suspensions were resuspended in FACS-buffer and labeled with CD31-microbeads
1058 (Miltenyi, 130-097-418) and enriched on MS-columns (Miltenyi, 130-042-201) according to
1059 manufacturer instructions. Cells were pelleted and lysed in RLT buffer. RNA was isolated
1060 using the RNeasy Micro Kit (Qiagen, 74004) and reverse transcribed using iScript cDNA
1061 synthesis kit (BioRad, 1708890) according to manufacturer instructions. qPCR was performed
1062 on a C1000 Touch thermal cycler equipped with a CFX384 detection module (Bio-Rad) with
1063 SYBR Green Master Mix reaction (Bio-Rad, 4367659) and the following PCR primer
1064 sequences (Sigma): *Gapdh* (F: TGTAGACCATGTAGTTGAGGTCA,

1065 R: AGGTGGTGTGAACGGATTG) *Pecam1* F: ACGCTGGTGCTCTATGCAAG, R:
1066 TCAGTTGCTGCCCATTCATCA) *Slc2a1* (F: CAGTCGGCTATAACACTGGTG, R:
1067 GCCCCCCACAGAGAAGATG) *Slc7a5* (F: CTTCGGCTCTGTCAATGGGT, R:
1068 TTCACCTTGATGGGACGCTC) *Mfsd2a* (F: AAAGACACGCAGAAAATGCTTACCT,
1069 R: AATGAAGGCACAGAGGGACGTAGA) *Gpihbp1* (F: AGGGCTGTCCTCCTGATCTTG,
1070 R: GGGTCCGCATCACCATCTT) *Slco2a1* (F: ATTAAGGTCTCGTGCCTTGTC, R:
1071 GTAGGCAGTAGAGCAACTG).

1072

1073 Human tissue

1074 Human lumbar dorsal root ganglia were obtained from organ donors through a collaboration
1075 with Transplant Quebec. All procedures are approved by and performed in accordance with
1076 the ethical review board at McGill University (*McGill University Health Centre REB 2019-*
1077 4896). Familial consent was obtained for each subject. Human DRGs were delivered frozen
1078 and prior to use were fixed in 4% formaldehyde for 3-6 hours followed by cryoprotection in
1079 30% sucrose for 3-5 days at 4°C. DRGs were embedded in OCT and sectioned at 12-50µm
1080 using a cryostat. Donor details are listed in Supplementary Table 1.

1081

1082 Analysis of publicly available data

1083 Raw or processed data from the following deposited studies were downloaded and re-
1084 clustered and analyzed using commercial code in the Bioturing Browser: Mouse DRG cells,
1085 GSE139103 (Avraham et al., 2020). Mouse sciatic nerve macrophages, GSE144707 (Ydens et
1086 al., 2020). Mouse multi-organ endothelial cells ArrayExpress: E-MTAB-8077 (Kalucka et al.,
1087 2020). Human DRG cells GSE169301 (Avraham et al., 2022). Enrichment scores for BBB
1088 and peripheral endothelium specific genes based on bulk RNA-seq of brain vs heart, lung,
1089 liver and kidney endothelial cells were retrieved from (Munji et al., 2019). Gene sets for *ex*
1090 *vivo* activation scores were retrieved from (Marsh et al., 2022)

1091

1092 Funding

1093 This work was supported by The Foundation Blanceflor (to H. Lund), Elisabeth och Alfred
1094 Ahlvists stiftelse (to H. Lund), David och Astrid Hageléns stiftelse (to H. Lund), The
1095 Swedish Brain Foundation (to H. Lund), Svenska Sällskapet för Medicinsk Forskning (to H.
1096 Lund), Wenner-Gren Foundation (to M. Hunt), Swedish Research Council grant 542-2013-
1097 8373 (to C. I. Svensson) and grant 2013-9306 (to J Lampå), the Knut and Alice Wallenberg
1098 Foundation (018.0161 and 2019.0437 to C. I. Svensson), the European Union Seventh
1099 Framework, European Union's Horizon 2020 research and innovation programme under the
1100 Marie Skłodowska-Curie Grant Agreement number 764860 (to C. I. Svensson), the European
1101 Research Council (ERC) under the European Union's Horizon 2020 research and innovation
1102 programme under the grant agreement no. 866075 (to C. I. Svensson), FOREUM (to C. I.
1103 Svensson), a generous donation from Leif Lundblad and family (to C. I. Svensson).

1104

1105 Acknowledgements

1106 We would like to thank the electron microscopy core facility EMil, Karolinska Institutet, for
1107 the TEM and SEM analysis. We acknowledge support for RNA sequencing from the National
1108 Genomics Infrastructure in Stockholm funded by Science for Life Laboratory

1109

1110

1111 References

1112

1113

- 1114 Ajami B, Bennett JL, Krieger C, Tetzlaff W, Rossi FMV. 2007. Local self-renewal can
1115 sustain CNS microglia maintenance and function throughout adult life. *Nat Neurosci*
1116 [Internet] 10:1538–1543. Available from:
1117 <http://eutils.ncbi.nlm.nih.gov/entrez/eutils/elink.fcgi?dbfrom=pubmed&id=18026097&retmode=ref&cmd=prlinks>
1118
- 1119 Amato AA, Ropper AH. 2020. Sensory Ganglionopathy. *New Engl J Med* 383:1657–1662.
- 1120 Andreone BJ, Chow BW, Tata A, Lacoste B, Ben-Zvi A, Bullock K, Deik AA, Ginty DD,
1121 Clish CB, Gu C. 2017. Blood-Brain Barrier Permeability Is Regulated by Lipid Transport-
1122 Dependent Suppression of Caveolae-Mediated Transcytosis. *Neuron* 94:581–594.e5.
- 1123 Anzil AP, Blinzingger K, Herrlinger H. 1976. Fenestrated blood capillaries in rat crano-spinal
1124 sensory ganglia. *Cell Tissue Res* 167:563–567.
- 1125 Armulik A, Genové G, Mäe M, Nisancioglu MH, Wallgard E, Niaudet C, He L, Norlin J,
1126 Lindblom P, Strittmatter K, Johansson BR, Betsholtz C. 2010. Pericytes regulate the
1127 blood–brain barrier. *Nature* 468:557–561.
- 1128 Arvidson B. 1979. Distribution of intravenously injected protein tracers in peripheral ganglia
1129 of adult mice. *Exp Neurol* 63:388–410.
- 1130 Avraham O, Chamessian A, Feng R, Yang L, Halevi AE, Moore AM, Gereau RW, Cavalli V.
1131 2022. Profiling the molecular signature of satellite glial cells at the single cell level reveals
1132 high similarities between rodents and humans. *Pain Publish Ahead of Print*.
- 1133 Avraham O, Deng P-Y, Jones S, Kuruvilla R, Semenkovich CF, Klyachko VA, Cavalli V.
1134 2020. Satellite glial cells promote regenerative growth in sensory neurons. *Nat Commun*
1135 11:4891.
- 1136 Bain CC, Bravo-Blas A, Scott CL, Perdigero EG, Geissmann F, Henri S, Malissen B,
1137 Osborne LC, Artis D, Mowat AM. 2014. Constant replenishment from circulating
1138 monocytes maintains the macrophage pool in the intestine of adult mice. *Nat Immunol*
1139 [Internet] 15:929–937. Available from: <http://www.nature.com/doifinder/10.1038/ni.2967>
- 1140 Blériot C, Chakarov S, Ginhoux F. 2020. Determinants of Resident Tissue Macrophage
1141 Identity and Function. *Immunity* 52:957–970.
- 1142 Bonnardel J, T'Jonck W, Gaublomme D, Browaeys R, Scott CL, Martens L, Vanneste B,
1143 Prijck SD, Nedospasov SA, Kremer A, Hamme EV, Borghgraef P, Toussaint W, Bleser
1144 PD, Mannaerts I, Beschin A, Grunsven LA van, Lambrecht BN, Taghon T, Lippens S,
1145 Elewaut D, Saeys Y, Guilliams M. 2019. Stellate Cells, Hepatocytes, and Endothelial Cells
1146 Imprint the Kupffer Cell Identity on Monocytes Colonizing the Liver Macrophage Niche.
1147 *Immunity* [Internet] 51:638–654.e9. Available from:
1148 <https://linkinghub.elsevier.com/retrieve/pii/S1074761319303681>
- 1149 Bulger RE, Eknayan G, Purcell DJ, Dobyan DC. 1983. Endothelial characteristics of
1150 glomerular capillaries in normal, mercuric chloride-induced, and gentamicin-induced acute
1151 renal failure in the rat. *J Clin Invest* 72:128–141.

- 1152 Chen L, Hua K, Zhang N, Wang J, Meng J, Hu Z, Gao H, Li F, Chen Y, Ren J, Liu L, Zhou
1153 Q, Gu J, Song J, Zhang X, Hu S. 2022. Multifaceted Spatial and Functional Zonation of
1154 Cardiac Cells in Adult Human Heart. *Circulation* 145:315–318.
- 1155 Devor M. 1999. Unexplained peculiarities of the dorsal root ganglion. *Pain* 82:S27–S35.
- 1156 Dick SA, Wong A, Hamidzada H, Nejat S, Nechanitzky R, Vohra S, Mueller B, Zaman R,
1157 Kantores C, Aronoff L, Momen A, Nechanitzky D, Li WY, Ramachandran P, Crome SQ,
1158 Becher B, Cybulsky MI, Billia F, Keshavjee S, Mital S, Robbins CS, Mak TW, Epelman
1159 S. 2022. Three tissue resident macrophage subsets coexist across organs with conserved
1160 origins and life cycles. *Sci Immunol* 7:eabf7777.
- 1161 Dzagnidze A, Katsarava Z, Makhalova J, Liedert B, Yoon M-S, Kaube H, Limmroth V,
1162 Thomale J. 2007. Repair Capacity for Platinum-DNA Adducts Determines the Severity of
1163 Cisplatin-Induced Peripheral Neuropathy. *J Neurosci* 27:9451–9457.
- 1164 Feng R, Saraswathy VM, Mokalled MH, Cavalli V. 2023. Self-renewing macrophages in
1165 dorsal root ganglia contribute to promote nerve regeneration. *Proc National Acad Sci*
1166 120:e2215906120.
- 1167 Gheorghe R-O, Grosu AV, Bica-Popi M, Ristoiu V. 2022. The Yin/Yang Balance of
1168 Communication between Sensory Neurons and Macrophages in Traumatic Peripheral
1169 Neuropathic Pain. *Int J Mol Sci* 23:12389.
- 1170 Ginhoux F, Greter M, Leboeuf M, Nandi S, See P, Gokhan S, Mehler MF, Conway SJ, Ng
1171 LG, Stanley ER, Samokhvalov IM, Merad M. 2010. Fate Mapping Analysis Reveals That
1172 Adult Microglia Derive from Primitive Macrophages. *Science* [Internet] 330:841–845.
1173 Available from: <http://www.sciencemag.org/cgi/doi/10.1126/science.1194637>
- 1174 Ginhoux F, Guilliams M. 2016. Tissue-Resident Macrophage Ontogeny and Homeostasis.
1175 *Immunity* [Internet] 44:439–449. Available from:
1176 <http://linkinghub.elsevier.com/retrieve/pii/S1074761316300632>
- 1177 Godel T, Pham M, Heiland S, Bendszus M, Bäumer P. 2016. Human dorsal-root-ganglion
1178 perfusion measured in-vivo by MRI. *Neuroimage* [Internet] 141:81–87. Available from:
1179 <https://linkinghub.elsevier.com/retrieve/pii/S1053811916303366>
- 1180 Goebel A, Krock E, Gentry C, Israel MR, Jurczak A, Urbina CM, Sandor K, Vastani N,
1181 Maurer M, Cuhadar U, Sensi S, Nomura Y, Menezes J, Bahapoor A, Brieskorn L,
1182 Sandström A, Tour J, Kadetoff D, Haglund L, Kosek E, Bevan S, Svensson CI, Andersson
1183 DA. 2021. Passive transfer of fibromyalgia symptoms from patients to mice. *J Clin Invest*
1184 131:e144201.
- 1185 Gosselin D, Link VM, Romanoski CE, Fonseca GJ, Eichenfield DZ, Spann NJ, Stender JD,
1186 Chun HB, Garner H, Geissmann F, Glass CK. 2014. Environment drives selection and
1187 function of enhancers controlling tissue-specific macrophage identities. *Cell* [Internet]
1188 159:1327–1340. Available from:
1189 <http://linkinghub.elsevier.com/retrieve/pii/S0092867414015001>

- 1190 Greene C, Hanley N, Campbell M. 2019. Claudin-5: gatekeeper of neurological function.
1191 Fluids Barriers Cns 16:3.
- 1192 Guilliams M, Thierry GR, Bonnardel J, Bajenoff M. 2020. Establishment and Maintenance of
1193 the Macrophage Niche. Immunity 52:434–451.
- 1194 Guimarães RM, Silva CEA da, Davoli-Ferreira M, Gomes FIF, Mendes A, Fonseca MM,
1195 Damasceno S, Andrade LP, Cunha FQ, Alves-Filho JC, Cunha TM. 2022. Sensory neuron-
1196 associated macrophages proliferate in the sensory ganglia after peripheral nerve injury in a
1197 CX3CR1 signaling dependent manner. Biorxiv:2022.03.22.485276.
- 1198 Guo L, Zhang H, Hou Y, Wei T, Liu J. 2016. Plasmalemma vesicle-associated protein: A
1199 crucial component of vascular homeostasis. Exp Ther Med 12:1639–1644.
- 1200 Gupta R, Bhaskar A. 2016. Chemotherapy-induced peripheral neuropathic pain. Bja Educ
1201 16:115–119.
- 1202 Haase R, Royer LA, Steinbach P, Schmidt D, Dibrov A, Schmidt U, Weigert M, Maghelli N,
1203 Tomancak P, Jug F, Myers EW. 2020. CLIJ: GPU-accelerated image processing for
1204 everyone. Nat Methods 17:5–6.
- 1205 Haberberger RV, Barry C, Dominguez N, Matusica D. 2019. Human Dorsal Root Ganglia.
1206 Front Cell Neurosci 13:271.
- 1207 Hanani M, Spray DC. 2020. Emerging importance of satellite glia in nervous system function
1208 and dysfunction. Nat Rev Neurosci 21:485–498.
- 1209 Hashimoto D, Chow A, Noizat C, Teo P, Beasley MB, Leboeuf M, Becker CD, See P, Price J,
1210 Lucas D, Greter M, Mortha A, Boyer SW, Forsberg EC, Tanaka M, Rooijen NV, García-
1211 Sastre A, Stanley ER, Ginhoux F, Frenette PS, Merad M. 2013. Tissue-Resident
1212 Macrophages Self-Maintain Locally throughout Adult Life with Minimal Contribution
1213 from Circulating Monocytes. Immunity [Internet] 38:792–804. Available from:
1214 <http://linkinghub.elsevier.com/retrieve/pii/S107476131300157X>
- 1215 He H, Mack JJ, c EG, Warren CM, Squadrito ML, Kilar斯基 WW, Baer C, Freshman RD,
1216 McDonald AI, Ziyad S, Swartz MA, Palma MD, Iruela-Arispe ML. 2016. Perivascular
1217 Macrophages Limit Permeability. Arteriosclerosis Thrombosis Vasc Biology [Internet]
1218 36:2203–2212. Available from:
1219 <https://www.ahajournals.org/doi/10.1161/ATVBAHA.116.307592>
- 1220 Hirakawa H, Okajima S, Nagaoka T, Kubo T, Takamatsu T, Oyamada M. 2004. Regional
1221 differences in blood–nerve barrier function and tight-junction protein expression within the
1222 rat dorsal root ganglion. Neuroreport 15:405–408.
- 1223 Hoeffel G, Chen J, Lavin Y, Low D, Almeida FF, See P, Beaudin AE, Lum J, Low I,
1224 Forsberg EC, Poidinger M, Zolezzi F, Larbi A, Ng LG, Chan JK, Greter M, Becher B,
1225 Samokhvalov IM, Merad M, Ginhoux F. 2015. C-Myb+ Erythro-Myeloid Progenitor-
1226 Derived Fetal Monocytes Give Rise to Adult Tissue-Resident Macrophages. Immunity
1227 [Internet] 42:665–678. Available from:
1228 <http://linkinghub.elsevier.com/retrieve/pii/S1074761315001259>

- 1229 Hunt MA, Lund H, Delay L, Santos GGD, Pham A, Kurtovic Z, Telang A, Lee A,
1230 Parvathaneni A, Kussick E, Corr M, Yaksh TL. 2022. DRGquant: A new modular AI-
1231 based pipeline for 3D analysis of the DRG. *J Neurosci Meth* 371:109497.
- 1232 Jacobs JM, Macfarlane RM, Cavanagh JB. 1976. Vascular leakage in the dorsal root ganglia
1233 of the rat, studied with horseradish peroxidase. *J Neurol Sci [Internet]* 29:95–107.
1234 Available from: <https://linkinghub.elsevier.com/retrieve/pii/0022510X76900836>
- 1235 Jimenez-Andrade JM, Herrera MB, Ghilardi JR, Vardanyan M, Melemedjian OK, Mantyh
1236 PW. 2008. Vascularization of the dorsal root ganglia and peripheral nerve of the mouse:
1237 implications for chemical-induced peripheral sensory neuropathies. *Mol Pain [Internet]*
1238 4:10. Available from: <http://journals.sagepub.com/doi/10.1186/1744-8069-4-10>
- 1239 Jung S, Aliberti J, Graemmel P, Sunshine MJ, Kreutzberg GW, Sher A, Littman DR. 2000.
1240 Analysis of Fractalkine Receptor CX 3 CR1 Function by Targeted Deletion and Green
1241 Fluorescent Protein Reporter Gene Insertion. *Mol Cell Biol* 20:4106–4114.
- 1242 Kalinski AL, Yoon C, Huffman LD, Duncker PC, Kohen R, Passino R, Hafner H, Johnson C,
1243 Kawaguchi R, Carbalal KS, Jara JS, Hollis E, Geschwind DH, Segal BM, Giger RJ. 2020.
1244 Analysis of the immune response to sciatic nerve injury identifies efferocytosis as a key
1245 mechanism of nerve debridement. *Elife* 9:e60223.
- 1246 Kalucka J, Rooij LPMH de, Goveia J, Rohlenova K, Dumas SJ, Meta E, Conchinha NV,
1247 Taverna F, Teuwen L-A, Veys K, García-Caballero M, Khan S, Geldhof V, Sokol L, Chen
1248 R, Treps L, Borri M, Zeeuw P de, Dubois C, Karakach TK, Falkenberg KD, Parys M, Yin
1249 X, Vinckier S, Du Y, Fenton RA, Schoonjans L, Dewerchin M, Eelen G, Thienpont B, Lin
1250 L, Bolund L, Li X, Luo Y, Carmeliet P. 2020. Single-Cell Transcriptome Atlas of Murine
1251 Endothelial Cells. *Cell [Internet]* 180:764-779.e20. Available from:
1252 <https://linkinghub.elsevier.com/retrieve/pii/S0092867420300623>
- 1253 Kiseleva RYU, Glassman PM, Greineder CF, Hood ED, Shuvaev VV, Muzykantov VR. 2018.
1254 Targeting therapeutics to endothelium: are we there yet? *Drug Deliv Transl Re* 8:883–902.
- 1255 Kobayashi S, Mwaka ES, Baba H, Takeno K, Miyazaki T, Matsuo H, Uchida K, Meir A.
1256 2010. Microvascular system of the lumbar dorsal root ganglia in rats. Part I: a 3D analysis
1257 with scanning electron microscopy of vascular corrosion casts: Laboratory investigation. *J*
1258 *Neurosurg Spine* 12:197–202.
- 1259 Kobayashi S, Yoshizawa H. 2002. Effect of mechanical compression on the vascular
1260 permeability of the dorsal root ganglion. *J Orthopaed Res* 20:730–739.
- 1261 Kolter J, Kierdorf K, Henneke P. 2020. Origin and Differentiation of Nerve-Associated
1262 Macrophages. *J Immunol* 204:271–279.
- 1263 Krock E, Morado-Urbina CE, Menezes J, Hunt MA, Sandström A, Kadetoff D, Tour J,
1264 Verma V, Kultima K, Haglund L, Meloto CB, Diatchenko L, Kosek E, Svensson CI. 2023.
1265 Fibromyalgia patients with elevated levels of anti-satellite glia cell immunoglobulin G
1266 antibodies present with more severe symptoms. *Pain Publish Ahead of Print*.

- 1267 Kutcher ME, Klagsbrun M, Mamluk R. 2004. VEGF is required for the maintenance of dorsal
1268 root ganglia blood vessels but not neurons during development. *Faseb J* 18:1952–1954.
- 1269 Kwon MJ, Kim J, Shin H, Jeong SR, Kang YM, Choi JY, Hwang DH, Kim BG. 2013.
1270 Contribution of macrophages to enhanced regenerative capacity of dorsal root ganglia
1271 sensory neurons by conditioning injury. *J Neurosci [Internet]* 33:15095–15108. Available
1272 from: <http://www.jneurosci.org/cgi/doi/10.1523/JNEUROSCI.0278-13.2013>
- 1273 Lavin Y, Winter D, Blecher-Gonen R, David E, Keren-Shaul H, Merad M, Jung S, Amit I.
1274 2014. Tissue-resident macrophage enhancer landscapes are shaped by the local
1275 microenvironment. *Cell [Internet]* 159:1312–1326. Available from:
1276 <http://linkinghub.elsevier.com/retrieve/pii/S0092867414014494>
- 1277 Laviña B, Castro M, Niaudet C, Cruys B, Álvarez-Aznar A, Carmeliet P, Bentley K,
1278 Brakebusch C, Betsholtz C, Gaengel K. 2018. Defective endothelial cell migration in the
1279 absence of Cdc42 leads to capillary-venous malformations. *Development* 145:dev161182.
- 1280 Lund H, Pieber M, Parsa R, Han J, Grommisch D, Ewing E, Kular L, Needhamen M,
1281 Espinosa A, Nilsson E, Överby AK, Butovsky O, Jagodic M, Zhang X-M, Harris RA.
1282 2018. Competitive repopulation of an empty microglial niche yields functionally distinct
1283 subsets of microglia-like cells. *Nat Commun [Internet]* 9:4845. Available from:
1284 <http://www.nature.com/articles/s41467-018-07295-7>
- 1285 Lux TJ, Hu X, Ben-Kraiem A, Blum R, Chen JT-C, Rittner HL. 2019. Regional Differences
1286 in Tight Junction Protein Expression in the Blood–DRG Barrier and Their Alterations after
1287 Nerve Traumatic Injury in Rats. *Int J Mol Sci* 21:270.
- 1288 Malong L, Napoli I, Casal G, White IJ, Stierli S, Vaughan A, Cattin A-L, Burden JJ, Hng KI,
1289 Bossio A, Flanagan A, Zhao HT, Lloyd AC. 2023. Characterization of the structure and
1290 control of the blood-nerve barrier identifies avenues for therapeutic delivery. *Dev Cell*
1291 58:174-191.e8.
- 1292 Marchetti GM, Burwell TJ, Peterson NC, Cann JA, Hanna RN, Li Q, Ongstad EL, Boyd JT,
1293 Kennedy MA, Zhao W, Rickert KW, Grimsby JS, Dall’Acqua WF, Wu H, Tsui P, Borrok
1294 MJ, Gupta R. 2019. Targeted drug delivery via caveolae-associated protein PV1 improves
1295 lung fibrosis. *Commun Biology* 2:92.
- 1296 Marsh SE, Walker AJ, Kamath T, Dissing-Olesen L, Hammond TR, Soysa TY de, Young
1297 AMH, Murphy S, Abdulraouf A, Nadaf N, Dufort C, Walker AC, Lucca LE, Kozareva V,
1298 Vanderburg C, Hong S, Bulstrode H, Hutchinson PJ, Gaffney DJ, Hafler DA, Franklin
1299 RJM, Macosko EZ, Stevens B. 2022. Dissection of artifactual and confounding glial
1300 signatures by single-cell sequencing of mouse and human brain. *Nat Neurosci* 25:306–316.
- 1301 Martínez-Lavín M. 2021. Dorsal root ganglia: fibromyalgia pain factory? *Clin Rheumatol*
1302 40:783–787.
- 1303 Mass E, Nimmerjahn F, Kierdorf K, Schlitzer A. 2023. Tissue-specific macrophages: how
1304 they develop and choreograph tissue biology. *Nat Rev Immunol*:1–17.

- 1305 Mildenberger W, Stifter SA, Greter M. 2022. Diversity and function of brain-associated
1306 macrophages. *Curr Opin Immunol* 76:102181.
- 1307 Miyata S. 2015. New aspects in fenestrated capillary and tissue dynamics in the sensory
1308 circumventricular organs of adult brains. *Front Neurosci-switz* 9:390.
- 1309 Molawi K, Wolf Y, Kandalla PK, Favret J, Hagemeyer N, Frenzel K, Pinto AR, Klapproth K,
1310 Henri S, Malissen B, Rodewald H-R, Rosenthal NA, Bajenoff M, Prinz M, Jung S,
1311 Sieweke MH. 2014. Progressive replacement of embryo-derived cardiac macrophages with
1312 age. *J Exp Medicine* [Internet] 211:2151–2158. Available from:
1313 <http://eutils.ncbi.nlm.nih.gov/entrez/eutils/elink.fcgi?dbfrom=pubmed&id=25245760&retmode=ref&cmd=prlinks>
1314
- 1315 Munji RN, Soung AL, Weiner GA, Sohet F, Semple BD, Trivedi A, Gimlin K, Kotoda M,
1316 Korai M, Aydin S, Batugal A, Cabangcala AC, Schupp PG, Oldham MC, Hashimoto T,
1317 Noble-Haeusslein LJ, Daneman R. 2019. Profiling the mouse brain endothelial
1318 transcriptome in health and disease models reveals a core blood-brain barrier dysfunction
1319 module. *Nat Neurosci* [Internet] 22:1892–1902. Available from:
1320 <http://www.nature.com/articles/s41593-019-0497-x>
- 1321 Nguyen LN, Ma D, Shui G, Wong P, Cazenave-Gassiot A, Zhang X, Wenk MR, Goh ELK,
1322 Silver DL. 2014. Mfsd2a is a transporter for the essential omega-3 fatty acid
1323 docosahexaenoic acid. *Nature* 509:503–506.
- 1324 Niemi JP, DeFrancesco-Lisowitz A, Roldán-Herández L, Lindborg JA, Mandell D, Zigmond
1325 RE. 2013. A critical role for macrophages near axotomized neuronal cell bodies in
1326 stimulating nerve regeneration. *J Neurosci* [Internet] 33:16236–16248. Available from:
1327 <http://www.jneurosci.org/cgi/doi/10.1523/JNEUROSCI.3319-12.2013>
- 1328 Nitta T, Hata M, Gotoh S, Seo Y, Sasaki H, Hashimoto N, Furuse M, Tsukita S. 2003. Size-
1329 selective loosening of the blood-brain barrier in claudin-5-deficient mice. *J Cell Biology*
1330 161:653–660.
- 1331 Ollion J, Cochennec J, Loll F, Escudé C, Boudier T. 2013. TANGO: a generic tool for high-
1332 throughput 3D image analysis for studying nuclear organization. *Bioinformatics* 29:1840–
1333 1841.
- 1334 Olsson Y. 1968. Topographical differences in the vascular permeability of the peripheral
1335 nervous system. *Acta Neuropathol* [Internet] 10:26–33. Available from:
1336 <http://link.springer.com/10.1007/BF00690507>
- 1337 Park MD, Silvin A, Ginhoux F, Merad M. 2022. Macrophages in health and disease. *Cell*
1338 185:4259–4279.
- 1339 Parton RG, McMahon K-A, Wu Y. 2020. Caveolae: Formation, dynamics, and function. *Curr*
1340 *Opin Cell Biol* 65:8–16.
- 1341 Peng J, Gu N, Zhou L, Eyo UB, Murugan M, Gan W-B, Wu L-J. 2016. Microglia and
1342 monocytes synergistically promote the transition from acute to chronic pain after nerve

- 1343 injury. *Nat Commun* [Internet] 7:12029. Available from:
1344 <http://www.nature.com/doifinder/10.1038/ncomms12029>
- 1345 Perdiguero EG, Klapproth K, Schulz C, Busch K, Azzoni E, Crozet L, Garner H, Trouillet C,
1346 Bruijn MF de, Geissmann F, Rodewald H-R. 2015. Tissue-resident macrophages originate
1347 from yolk-sac-derived erythro-myeloid progenitors. *Nature* [Internet] 518:547–551.
1348 Available from: <http://www.nature.com/doifinder/10.1038/nature13989>
- 1349 Potente M, Mäkinen T. 2017. Vascular heterogeneity and specialization in development and
1350 disease. *Nat Rev Mol Cell Bio* 18:477–494.
- 1351 Profaci CP, Munji RN, Pulido RS, Daneman R. 2020. The blood–brain barrier in health and
1352 disease: Important unanswered questions. *J Exp Med* 217:e20190062.
- 1353 Raoof R, Gil CM, Lafeber FPJG, Visser H de, Prado J, Versteeg S, Pascha MN, Heinemans
1354 ALP, Adolfs Y, Pasterkamp J, Wood JN, Mastbergen SC, Eijkelkamp N. 2021. Dorsal
1355 Root Ganglia Macrophages Maintain Osteoarthritis Pain. *J Neurosci* 41:8249–8261.
- 1356 Razani B, Engelman JA, Wang XB, Schubert W, Zhang XL, Marks CB, Macaluso F, Russell
1357 RG, Li M, Pestell RG, Vizio DD, Hou H, Kneitz B, Lagaud G, Christ GJ, Edelmann W,
1358 Lisanti MP. 2001. Caveolin-1 Null Mice Are Viable but Show Evidence of
1359 Hyperproliferative and Vascular Abnormalities*. *J Biol Chem* 276:38121–38138.
- 1360 Reinhold AK, Rittner HL. 2020. Characteristics of the nerve barrier and the blood dorsal root
1361 ganglion barrier in health and disease. *Exp Neurol* 327:113244.
- 1362 Renier N, Wu Z, Simon DJ, Yang J, Ariel P, Tessier-Lavigne M. 2014. iDISCO: A Simple,
1363 Rapid Method to Immunolabel Large Tissue Samples for Volume Imaging. *Cell* 159:896–
1364 910.
- 1365 Richards M, Nwadozi E, Pal S, Martinsson P, Kaakinen M, Gloger M, Sjöberg E, Koltowska
1366 K, Betsholtz C, Eklund L, Nordling S, Claesson-Welsh L. 2022. Claudin5 protects the
1367 peripheral endothelial barrier in an organ and vessel-type-specific manner. *Elife*
1368 11:e78517.
- 1369 Richner M, Ferreira N, Dudele A, Jensen TS, Vaegter CB, Gonçalves NP. 2019. Functional
1370 and Structural Changes of the Blood-Nerve-Barrier in Diabetic Neuropathy. *Front
1371 Neurosci-switz* 12:1038.
- 1372 Ronneberger O, Fischer P, Brox T. 2015. U-Net: Convolutional Networks for Biomedical
1373 Image Segmentation. Arxiv.
- 1374 Sanin DE, Ge Y, Marinkovic E, Kabat AM, Castoldi A, Caputa G, Grzes KM, Curtis JD,
1375 Thompson EA, Willenborg S, Dichtl S, Reinhardt S, Dahl A, Pearce EL, Eming SA,
1376 Gerbaulet A, Roers A, Murray PJ, Pearce EJ. 2022. A common framework of monocyte-
1377 derived macrophage activation. *Sci Immunol* 7:eabl7482.
- 1378 Satchell SC, Braet F. 2009. Glomerular endothelial cell fenestrations: an integral component
1379 of the glomerular filtration barrier. *Am J Physiol-renal* 296:F947–F956.

- 1380 Schindelin J, Arganda-Carreras I, Frise E, Kaynig V, Longair M, Pietzsch T, Preibisch S,
1381 Rueden C, Saalfeld S, Schmid B, Tinevez J-Y, White DJ, Hartenstein V, Eliceiri K,
1382 Tomancak P, Cardona A. 2012. Fiji: an open-source platform for biological-image
1383 analysis. *Nat Methods* 9:676–682.
- 1384 Schmidt U, Weigert M, Broaddus C, Myers G. 2018. Medical Image Computing and
1385 Computer Assisted Intervention – MICCAI 2018, 21st International Conference, Granada,
1386 Spain, September 16-20, 2018, Proceedings, Part II. *Lect Notes Comput Sc*:265–273.
- 1387 Schulz C, Perdiguero EG, Chorro L, Szabo-Rogers H, Cagnard N, Kierdorf K, Prinz M, Wu
1388 B, Jacobsen SEW, Pollard JW, Frampton J, Liu KJ, Geissmann F. 2012. A Lineage of
1389 Myeloid Cells Independent of Myb and Hematopoietic Stem Cells. *Science* [Internet]
1390 336:86–90. Available from: <http://www.sciencemag.org/cgi/doi/10.1126/science.1219179>
- 1391 Serbina NV, Pamer EG. 2006. Monocyte emigration from bone marrow during bacterial
1392 infection requires signals mediated by chemokine receptor CCR2. *Nat Immunol* [Internet]
1393 7:311–317. Available from: <http://www.nature.com/doifinder/10.1038/ni1309>
- 1394 Shaw TN, Houston SA, Wemyss K, Bridgeman HM, Barbera TA, Zangerle-Murray T,
1395 Strangward P, Ridley AJL, Wang P, Tamoutounour S, Allen JE, Konkel JE, Grainger JR.
1396 2018. Tissue-resident macrophages in the intestine are long lived and defined by Tim-4
1397 and CD4 expression. *J Exp Med* 215:1507–1518.
- 1398 Silva HM, Kitoko JZ, Queiroz CP, Kroehling L, Matheis F, Yang KL, Reis BS, Ren-Fielding
1399 C, Littman DR, Bozza MT, Mucida D, Lafaille JJ. 2021. c-MAF-dependent perivascular
1400 macrophages regulate diet-induced metabolic syndrome. *Sci Immunol* 6:eabg7506.
- 1401 Singh SK, Kruckowski K, Laumet GO, Weis D, Alexander JF, Heijnen CJ, Kavelaars A. 2022.
1402 CD8+ T cell-derived IL-13 increases macrophage IL-10 to resolve neuropathic pain. *Jci*
1403 Insight 7:e154194.
- 1404 Srinivas S, Watanabe T, Lin C-S, William CM, Tanabe Y, Jessell TM, Costantini F. 2001.
1405 Cre reporter strains produced by targeted insertion of EYFP and ECFP into the ROSA26
1406 locus. *Bmc Dev Biol* 1:4.
- 1407 Stan R-V, Kubitz M, Palade GE. 1999. PV-1 is a component of the fenestral and stomatal
1408 diaphragms in fenestrated endothelia. *Proc National Acad Sci* 96:13203–13207.
- 1409 Stan RV, Tkachenko E, Niesman IR. 2004. PV1 Is a Key Structural Component for the
1410 Formation of the Stomatal and Fenestral Diaphragms. *Mol Biol Cell* 15:3615–3630.
- 1411 Tamoutounour S, Henri S, Lelouard H, Bovis B de, Haar C de, Woude CJ van der, Woltman
1412 AM, Reyal Y, Bonnet D, Sichien D, Bain CC, Mowat AM, Sousa CR e, Poulin LF,
1413 Malissen B, Guilliams M. 2012. CD64 distinguishes macrophages from dendritic cells in
1414 the gut and reveals the Th1-inducing role of mesenteric lymph node macrophages during
1415 colitis. *Eur J Immunol* [Internet] 42:3150–3166. Available from:
1416 <http://doi.wiley.com/10.1002/eji.201242847>
- 1417 Trimm E, Red-Horse K. 2022. Vascular endothelial cell development and diversity. *Nat Rev*
1418 *Cardiol*:1–14.

- 1419 Ubogu EE. 2020. Biology of the human blood-nerve barrier in health and disease. *Exp Neurol*
1420 328:113272.
- 1421 Vanlandewijck M, He L, Mäe MA, Andrae J, Ando K, Gaudio FD, Nahar K, Lebouvier T,
1422 Laviña B, Gouveia L, Sun Y, Raschperger E, Räsanen M, Zarb Y, Mochizuki N, Keller
1423 A, Lendahl U, Betsholtz C. 2018. A molecular atlas of cell types and zonation in the brain
1424 vasculature. *Nature* [Internet] 554:475–480. Available from:
1425 <http://www.nature.com/articles/nature25739>
- 1426 Vlist M van der, Raoof R, Willemen HLDM, Prado J, Versteeg S, Gil CM, Vos M, Lokhorst
1427 RE, Pasterkamp RJ, Kojima T, Karasuyama H, Khouri-Hanold W, Meyaard L,
1428 Eijkelkamp N. 2022. Macrophages transfer mitochondria to sensory neurons to resolve
1429 inflammatory pain. *Neuron* 110:613–626.e9.
- 1430 Wang PL, Yim AKY, Kim K-W, Avey D, Czepielewski RS, Colonna M, Milbrandt J,
1431 Randolph GJ. 2020a. Peripheral nerve resident macrophages share tissue-specific
1432 programming and features of activated microglia. *Nat Commun* 11:2552.
- 1433 Wang Z, Liu C-H, Huang S, Fu Z, Tomita Y, Britton WR, Cho SS, Chen CT, Sun Y, Ma J,
1434 He X, Chen J. 2020b. Wnt signaling activates MFSD2A to suppress vascular endothelial
1435 transcytosis and maintain blood-retinal barrier. *Sci Adv* 6:eaba7457.
- 1436 Willis CL, Garwood CJ, Ray DE. 2007. A size selective vascular barrier in the rat area
1437 postrema formed by perivascular macrophages and the extracellular matrix. *Neuroscience*
1438 150:498–509.
- 1439 Yang AC, Vest RT, Kern F, Lee DP, Agam M, Maat CA, Losada PM, Chen MB, Schaum N,
1440 Khouri N, Toland A, Calcuttawala K, Shin H, Pálovics R, Shin A, Wang EY, Luo J, Gate
1441 D, Schulz-Schaeffer WJ, Chu P, Siegenthaler JA, McNerney MW, Keller A, Wyss-Coray
1442 T. 2022. A human brain vascular atlas reveals diverse mediators of Alzheimer's risk.
1443 *Nature* 603:885–892.
- 1444 Ydens E, Amann L, Asselbergh B, Scott CL, Martens L, Sichien D, Mossad O, Blank T,
1445 Prijck SD, Low D, Masuda T, Saeys Y, Timmerman V, Stumm R, Ginhoux F, Prinz M,
1446 Janssens S, Guilliams M. 2020. Profiling peripheral nerve macrophages reveals two
1447 macrophage subsets with distinct localization, transcriptome and response to injury. *Nat
1448 Neurosci* 23:676–689.
- 1449 Yim AKY, Wang PL, Bermingham JR, Hackett A, Strickland A, Miller TM, Ly C, Mitra RD,
1450 Milbrandt J. 2022. Disentangling glial diversity in peripheral nerves at single-nuclei
1451 resolution. *Nat Neurosci* 25:238–251.
- 1452 Yona S, Kim K-W, Wolf Y, Mildner A, Varol D, Breker M, Strauss-Ayali D, Viukov S,
1453 Guilliams M, Misharin A, Hume DA, Perlman H, Malissen B, Zelzer E, Jung S. 2013. Fate
1454 Mapping Reveals Origins and Dynamics of Monocytes and Tissue Macrophages under
1455 Homeostasis. *Immunity* [Internet] 38:79–91. Available from:
1456 <http://linkinghub.elsevier.com/retrieve/pii/S1074761312005481>
- 1457 Yu X, Liu H, Hamel KA, Morvan MG, Yu S, Leff J, Guan Z, Braz JM, Basbaum AI. 2020.
1458 Dorsal root ganglion macrophages contribute to both the initiation and persistence of

- 1459 neuropathic pain. *Nat Commun* [Internet] 11:264. Available from:
1460 <http://www.nature.com/articles/s41467-019-13839-2>
- 1461 Zhang H, Li Y, Carvalho-Barbosa M de, Kavelaars A, Heijnen CJ, Albrecht PJ, Dougherty
1462 PM. 2016. Dorsal Root Ganglion Infiltration by Macrophages Contributes to~Paclitaxel
1463 Chemotherapy-Induced Peripheral Neuropathy. *J Pain* [Internet] 17:775–786. Available
1464 from: <http://linkinghub.elsevier.com/retrieve/pii/S1526590016005629>
- 1465 Zhang W, Dai M, Fridberger A, Hassan A, DeGagne J, Neng L, Zhang F, He W, Ren T,
1466 Trune D, Auer M, Shi X. 2012. Perivascular-resident macrophage-like melanocytes in the
1467 inner ear are essential for the integrity of the intrastrial fluid–blood barrier. *Proc National
1468 Acad Sci* 109:10388–10393.
- 1469 Zhao Z, Nelson AR, Betsholtz C, Zlokovic BV. 2015. Establishment and Dysfunction of the
1470 Blood-Brain Barrier. *Cell* 163:1064–1078.
- 1471 Zigmond RE, Echevarria FD. 2019. Macrophage biology in the peripheral nervous system
1472 after injury. *Prog Neurobiol* [Internet] 173:102–121. Available from:
1473 <https://linkinghub.elsevier.com/retrieve/pii/S030100821830128X>
- 1474